ACS OMEGA

http://pubs.acs.org/journal/acsodf

Article

Deciphering the Precise Target for Saroglitazar Associated Antiangiogenic Effect: A Computational Synergistic Approach

Swarna Dabral, Imran Ahmd Khan, Tarun Pant, Sabina Khan, Prem Prakash, Suhel Parvez, and Nilanjan Saha*

Cite This: *ACS Omega* 2023, 8, 14985−15002

Read Online

ACCESS | Metrics & More | Article Recommendations | Supporting Information

ABSTRACT: Antidiabetic drugs that have a secondary pharmacological effect on angiogenesis inhibition may help diabetic patients delay or avoid comorbidities caused by angiogenesis including malignancies. In recent studies, saroglitazar has exhibited antiangiogenic effects in diabetic retinopathy. The current study investigates the antiangiogenic effects of saroglitazar utilizing the chicken chorioallantoic membrane (CAM) assay and then identifies its precise mode of action on system-level protein networks. To determine the regulatory effect of saroglitazar on the protein−protein interaction network (PIN), 104 target genes were retrieved and tested using an acid server and Swiss target prediction tools. A string-based interactome was created and analyzed using Cytoscape. It was determined that the constructed network was scale-free, making it biologically relevant. Upon topological analysis of the network, 37 targets were screened on the basis of centrality values. Submodularization of the interactome resulted in the formation of four clusters. A total of 20 common targets identified in topological analysis and modular analysis were filtered. A total of 20 targets were compiled and were integrated into the pathway enrichment analysis using ShinyGO. The majority of hub genes were associated with cancer and PI3-AKT signaling pathways. Molecular docking was utilized to reveal the most potent target, which was validated by using molecular dynamic simulations and immunohistochemical staining on the chicken CAM. The comprehensive study offers an alternate research paradigm for the investigation of antiangiogenic effects using CAM assays. This was followed by the identification of the precise off-target use of saroglitazar using system biology and network pharmacology to inhibit angiogenesis.

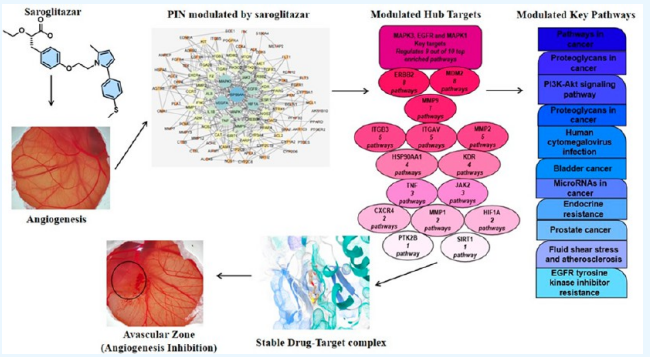

1. INTRODUCTION

Diabetes mellitus has been one of the most prominent and rapidly propagating global health problems, with incidences of impaired glucose tolerance reaching nearly epidemic proportions. Type 2 diabetes mellitus (T2DM) commonly occurs in 4.7% to 8.5% of the world's population, affecting 300 million people worldwide, and the prevalence of this disease is expected to affect 700 million in the next several decades. The increasing incidences of T2DM in recent decades can be attributed to several factors, such as genetic predisposition, epigenetic changes, lower consumption of a fiber-rich diet, lack of physical activity, and exposure to environmental stressors.[1−4] In the past few years, epidemiological and pathological data have depicted that diabetes is a significant predictor of macrovascular complications.[5−9] Additionally, substantial studies have shown an association between diabetes and cancer, suggesting that diabetic patients are at high risk of developing cancer.[10−15] Multiple studies have also shown that various herbal compounds, such as ginseng, mulberry, and oolong tea, can inhibit the progression of both diabetes and tumors, implying that the two diseases share a common pathology and, as a result, treatment targets.[16−18]

Moreover, the development of diabetes and cancer involves dysregulation of standard physiological processes such as angiogenesis.[19] However, even with this extensive research, our understanding of the mechanisms driving this bidirectional development of cancer and diabetes remains enigmatic.

Angiogenesis is the formation of new blood vessels from pre-existing ones, facilitating adequate oxygen and nutrients to the growing tissues and organs.[20] Several studies have shown that alteration of physiological angiogenesis can foster the development of several pathological diseases, including cancer and diabetes.[16] However, the lack of potential therapeutic options imposes a significant challenge to preventing disease develop-

Received: November 26, 2022
Accepted: February 13, 2023
Published: April 20, 2023

ment. In the past few years, traditional antiangiogenic therapies have gained partial success as most of them were found to enhance tumor invasiveness.[21] Recent advancements in pharmacology have allowed researchers to use novel non-thiazolidinedione (TZD) compounds such as saroglitazar for treating diabetic retinopathy via mitigating angiogenesis.[8] Despite these past studies, the precise target by which saroglitazar modulates angiogenesis and the critical pathways associated with it are unknown. The current study sought to investigate the antiangiogenic potential of saroglitazar. For the exploration of the angiogenic modulatory effect of saroglitazar, a chicken chorioallantoic membrane (CAM) assay was utilized. This exploratory study is followed by an analysis of the regulatory genes in the saroglitazar interactome that may be involved in altering the mechanism of angiogenesis. To seek the potential targets of saroglitazar and the gene associated with angiogenesis, we conducted target fishing. Additionally, molecular docking and dynamic simulation analysis were performed to screen for validation of the most probable and critical regulators of pathways that might be contributing to angiogenesis. Furthermore, we validated the findings from the bioinformatic analyses via the immunohistochemical examination of the CAM membrane for the measurement of the expression of angiogenesis-related proteins. This study proposes an alternative preclinical research paradigm for exploration of the angiogenesis inhibitors, target identification by utilizing system biology and computational tools as synergistic tools and validation by using the CAM assay for angiogenesis research.

2. RESULTS

2.1. Saroglitzar Inhibited Blood Vessel Development *In Ovo*. *In ovo* exposure to saroglitazar inhibited the physiological angiogenesis in the CAM of the chicken embryo. Antiangiogenic effects were demonstrated via avascular zones in the CAM in a dose-dependent manner (see Figure 1). Examining the avascular sections of the membranes, it was observed that 0.2 and 2 $\mu g/\mu L$ saroglitazar had a powerful antiangiogenic effect, with scores of 1.5 and 1.8, respectively, whereas 0.06 $\mu g/\mu L$ saroglitazar exhibited a good antiangiogenic effect with an average antiangiogenic score of 1.3.

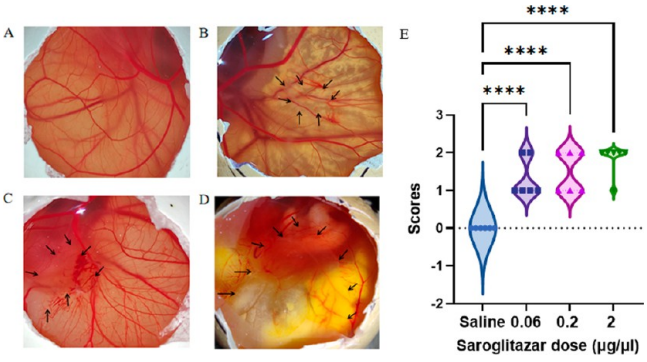

Figure 1. Figure illustrates the avascular zones in the chicken CAM after saroglitazar administration in a dose-dependent manner. CAM after: A: vehicle administration; B: saroglitazar 0.06 $\mu g/\mu L$; C: saroglitazar 0.2 $\mu g/\mu L$; D: saroglitazar 2 $\mu g/\mu L$. The black arrows represent avascular zones (angiogenesis inhibition) in the CAMs. E: Semiquantitative scores after angiogenesis inhibition; $n = 6$, ****$p < 0.0001$.

2.2. Identification of Putative Targets of Saroglitazar. A total of 109 and 492 targets for saroglitazar were identified using Swiss target prediction tools and the ACID server, respectively. After the removal of the duplicates from the total of 601 (492 + 109), a total of 522 targets associated with saroglitazar were obtained.

2.3. Identification of Targets Associated with Angiogenesis. From TTD, the DrugBank database, and DisGenet, a total of 908 genes were found to be linked to tumor-driven or pathological angiogenesis.

2.4. Construction and Visualization of a Protein–Protein Interaction Network (PIN). The intersection (104 targets) between drug (saroglitazar) and disease (angiogenesis) obtained from Gene Venn is presented in Figure 2(A). A total of 104 genes were screened as predicted targets of saroglitazar in modulating angiogenesis. A PPI network was constructed using the string database. Targets at the intersection exhibited 404 edges, representing the interaction among the targets (104 nodes and 404 edges) (Supplementary Figure S1).

2.5. Topological Analysis of PINs. The network obtained from the string was subsequently analyzed and visualized in the Network Analyzer plugin in Cytoscape. Following the analysis in Cytoscape, topological properties of the network like node degree distribution, characteristic path length, and clustering coefficient were evaluated. In the current study, the degree exponent was calculated as 0.833 through fitting the node degree distribution curve. Furthermore, the path length is a network property that indicates that the information in the network travels at an accelerated pace. The clustering coefficient represents the closeness of nodes and is used to identify the tendency of nodes to form functional modules in the network.[22] The characteristic path length and clustering coefficient of the saroglitazar-rewired PIN were 2.721 and 0.431, respectively. The identification of the top 37 key nodes was screened via node degree and closeness centrality. A cutoff value of node degree >8 and closeness centrality (CC) > 0.382 were considered as topological parameters for gene prioritization. The hub genes in the network based on the cutoff values are presented in Table S1. Among these, HSP90AA1 is the superhub gene that has the highest CC and degree in the network (see Figure 2 B and Table S1). Furthermore, gene prioritization was also done through the modularization of the network.

2.6. Modular Analysis of PIN. After topological analysis of the network, MCODE analysis in Cytoscape was performed to identify densely connected regions. The identified targets were clustered into four modules: Cluster 1 (10 nodes and 21 edges): HIF1A, BRAF, HDAC2, SIRT1, MDM2, MAPK1, HSP90AA1, NTRK1, PARP1, CXCR4; Cluster 2 (12 nodes and 22 edges): ICAM1, JAK2, PTK2B, MMP2, MMP9, TNF, KDR, ITGAV, ERBB2, MET, ITGB3, MMP1; Cluster 3 (8 nodes and 14 edges): CYP1A2, ALB, MAPK3, CYP2C9, CYP3A4, CYP2C19, CYP2C8, EGFR; Cluster 4 (8 nodes and 9 edges): ESR1, VEGFA, ILIB, BCL2, FGF3, FGF4, MCL1, NOS2, which represent highly interconnected targets (see Figure 2 C).

2.7. Functional Enrichment Analysis. For the elaboration of the biological functions, the characterized hub targets were subjected to GO and KEGG pathway enrichment analyses. A total of 20 targets were integrated for the GO and pathway analysis. These 20 targets were screened as hubs following topological analysis of the network and were also

https://doi.org/10.1021/acsomega.2c07570
ACS Omega 2023, 8, 14985−15002

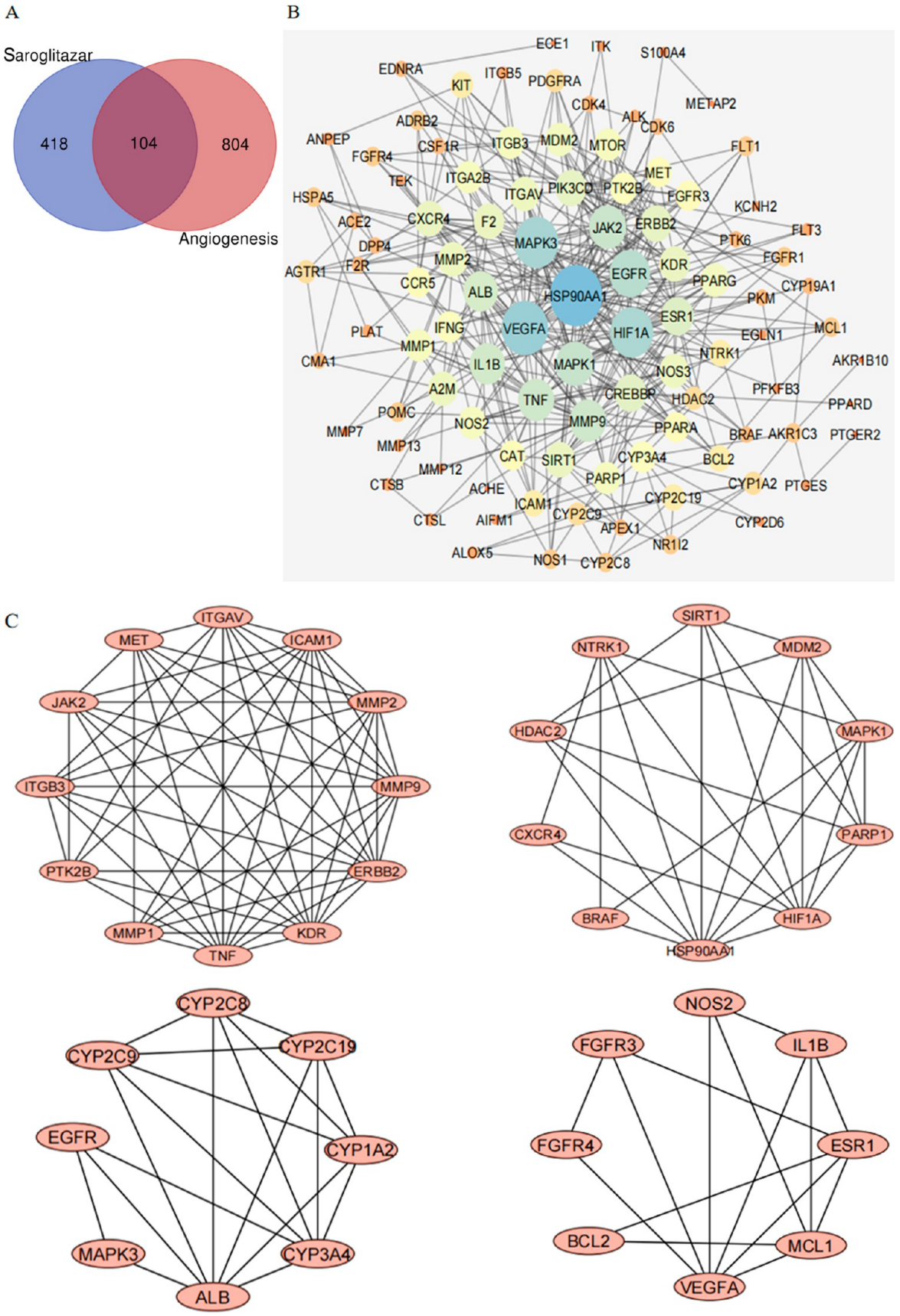

Figure 2. A: Intersection of common targets of saroglitazar and angiogenesis. B: Protein−protein interaction network (PIN) of saroglitazar rewired 104 common proteins analyzed via Cytoscape. The size and color of the circle varied with the degree values of the nodes. Higher degrees are represented as larger nodes and brighter colors. C: Clusters obtained from modular analysis using MCODE

https://doi.org/10.1021/acsomega.2c07570
ACS Omega 2023, 8, 14985−15002

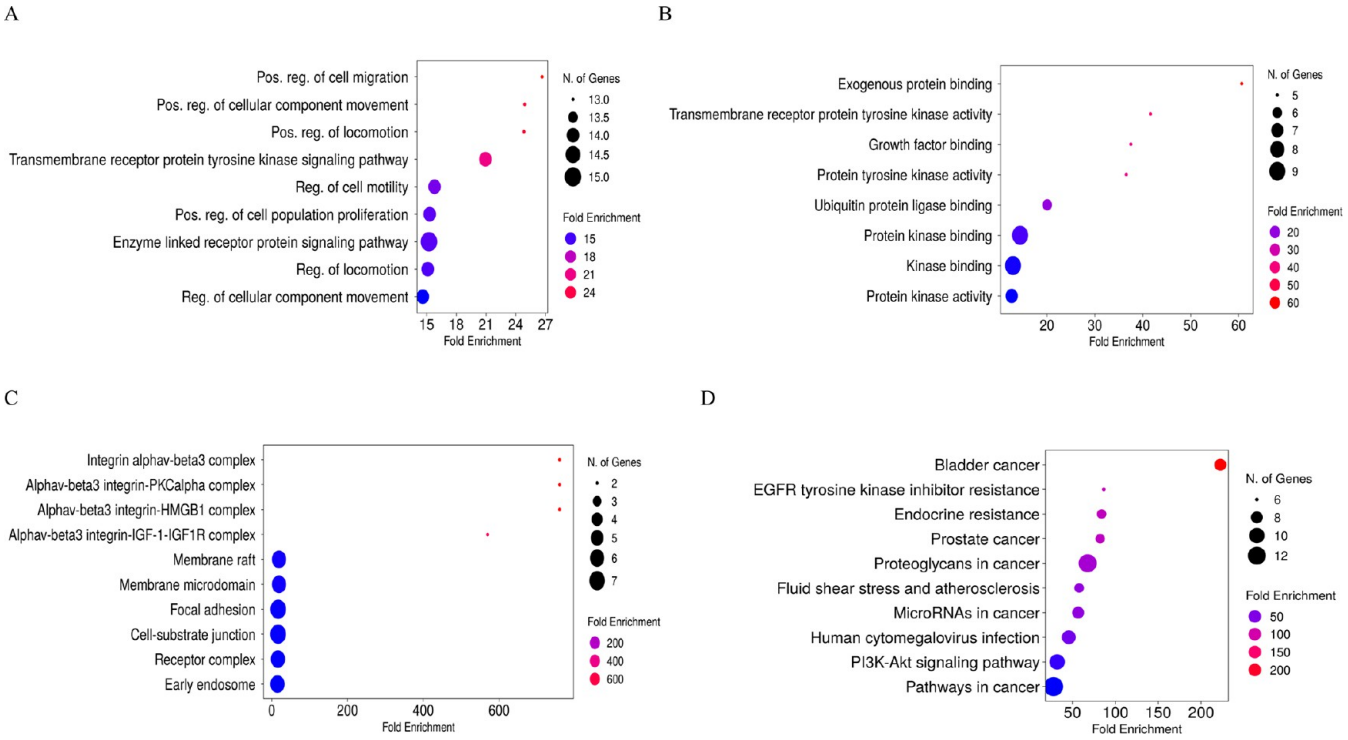

Figure 3. Gene ontology enrichment analysis: The *Y*-axis represents the identified GO categories in the analysis and the X-axis represents the fold enrichment. The bigger size of the red, purple, and blue dots represents more numbers of genes in these categories. A: Enrichment representation of the top 10 pathways in biological processes. B: Enrichment representation of the top 10 pathways in molecular function. C: Enrichment representation of the top 10 pathways in cellular components. D: KEGG pathway enrichment analysis: The *y*-axis represents the pathway term, and the *x*-axis represents the fold enrichment in each KEGG pathway. The bigger sizes of red, purple, and blue color dots represent more number of genes. Abbreviations: Pos.: Positive; Reg.: Regulation; N. of Genes: number of genes; no.: Number.

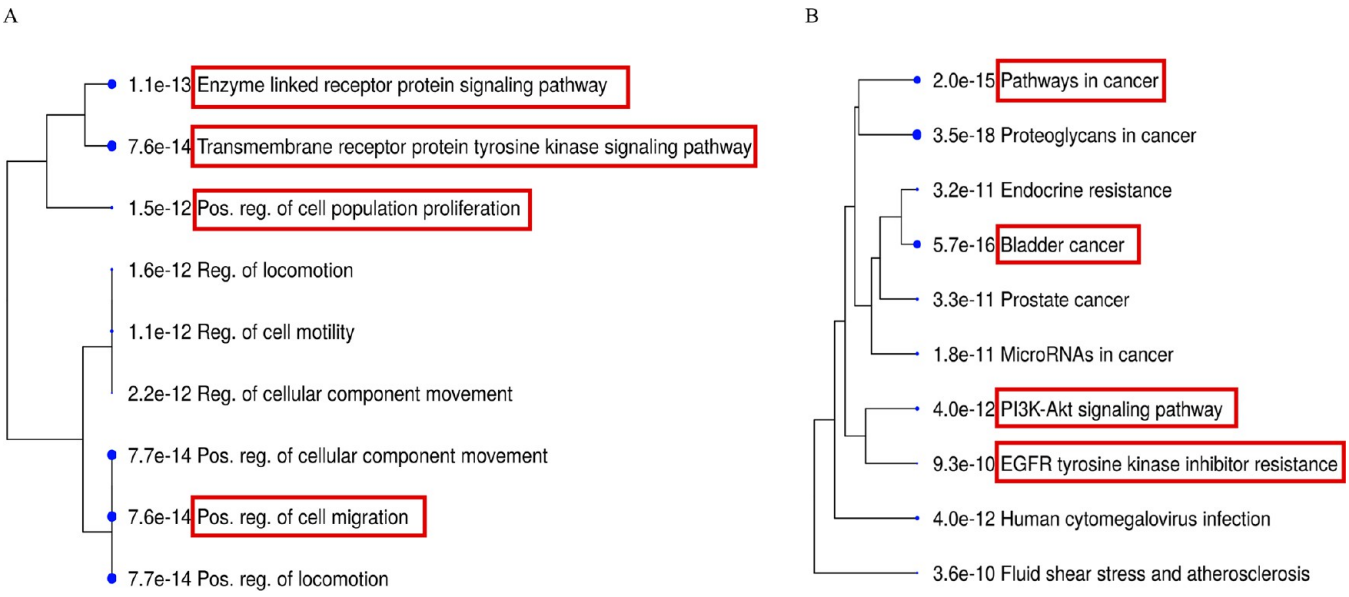

Figure 4. Hierarchical clustering tree summarizes the correlation among significant pathways listed in the enrichment tab. A: Biological Process. B: Biological pathways. Pathways with many shared genes are clustered together. Bigger dots indicate more significant P-values.

identified in clusters after modulation of the network. In GO analysis, a total of 403 GO terms were identified, including 355 terms of Biological Process (BP), 27 terms of Molecular Function (MF), and 21 terms of Cell Composition (CC), accounting for 88.09%, 6.7%, and 5.21%, respectively. The top 10 BP, MF, and CC are visualized in Figures 3A−C, respectively. Fold enrichment in the chart shows how considerably the genes of a certain pathway are over-represented.

The chart presented illustrated that BP was significantly enriched with positive regulation of (i) cell migration, (ii) cell component movement, (iii) locomotion, (iv) transmembrane receptor protein, (v) tyrosine kinase signaling pathway, (vi) regulation of cell motility, etc. (see Figure 3A). The correlation

https://doi.org/10.1021/acsomega.2c07570
ACS Omega 2023, 8, 14985−15002

between these processes are illustrated in Figure 4A. The main GO terms for MF were related to (i) exogenous protein binding, (ii) transmembrane receptor protein tyrosine kinase activity, (iii) growth factor binding, (iv) protein tyrosine kinase activity, etc. (see Figure 3B). CC were enriched in (i) integrin alphav-beta3 (av-b3) complex, (ii) av-b3 integrin-PKCa complex, (iii) av-b3 integrin HMGB1 complex, (iv) av-b3 integrin IGF-1-IGF-R-1 complex, and so on (see Figure 3C).

The essential signaling pathways of saroglitazar in angiogenesis were presented by KEGG pathway enrichment analysis. A total of 92 pathways were significantly associated with saroglitazar as a target (p value < 0.01). The top 10 pathways are displayed in Figure 3D. Common signaling pathways primarily focus on bladder cancer, EGFR-tyrosine kinase inhibitor resistance, endocrine resistance, prostate cancer, proteoglycans in cancer, fluid shear stress, and atherosclerosis; MicroRNAs in cancer; human cytomegalovirus infection; PI3K-Akt signaling pathway; and cancer pathways. The details of genes associated with the following pathways are listed in Table 1. The correlation between these pathways are illustrated in Figure 4B. The full form of all hub genes is in Table S2.

Table 1. List of Pathways with Associated Genes

no.	pathway	n. genes	genes
1	pathways in cancer	13	HSP90AA1 MMP2 JAK2 MAPK1 HIF1A MMP9 MAPK3 CXCR4 MDM2 ITGAV ERBB2 EGFR MMP1
2	proteoglycans in cancer	12	MMP2 MAPK1 HIF1A MMP9 MAPK3 KDR MDM2 ITGAV ERBB2 EGFR TNF ITGB3
3	PI3K-Akt signaling pathway	10	HSP90AA1 JAK2 MAPK1 MAPK3 KDR MDM2 ITGAV ERBB2 EGFR ITGB3
4	human cytomegalovirus infection	9	MAPK1 MAPK3 PTK2B CXCR4 MDM2 ITGAV EGFR TNF ITGB3
5	bladder cancer	8	MMP2 MAPK1 MMP9 MAPK3 MDM2 ERBB2 EGFR MMP1
6	MicroRNAs in cancer	8	SIRT1 MAPK1 MMP9 MAPK3 MDM2 ERBB2 EGFR ITGB3
7	endocrine resistance	7	MMP2 MAPK1 MMP9 MAPK3 MDM2 ERBB2 EGFR
8	prostate cancer	7	HSP90AA1 MAPK1 MMP9 MAPK3 MDM2 ERBB2 EGFR
9	fluid shear stress and atherosclerosis	7	HSP90AA1 MMP2 MMP9 KDR ITGAV TNF ITGB3
10	EGFR tyrosine kinase inhibitor resistance	6	JAK2 MAPK1 MAPK3 KDR ERBB2 EGFR

2.8. Compound−Target−Pathway Interaction. A compound−target−pathway interaction network was established, as presented in Figure 5. The hexagon represents the compound, the ellipse represents the gene targets, and the V shape represents the pathways. The network had 31 nodes and 107 edges (see Figure 5). Among the associated targets, MAPK3, EGFR, and MAPK1 were associated with the highest number of top 10 pathways, i.e., 9 pathways, followed by ERBB2; 8, MDM2; 8, MMP9; 7, ITGB3; 5, ITGAV; 5, MMP2; 5, HSP90AA1; 4, KDR; 4, TNF; 3, JAK2; 3, CXCR4; 2,; MMP1; 2, HIF1A 2, PTK2B; 1 and SIRT1; 1 pathway.

2.9. Molecular Docking Analysis. Molecular docking was performed on hub targets identified via topological analysis of the network and via modular analysis using MCODE. A total of 20 proteins were docked with saroglitazar. The details of the binding affinities of saroglitazar with these targets are presented in Table 2.

2.9.1. Interaction of Saroglitazar with EGFR. The active pocket of the EGFR comprises the following amino acid residues: Phe 997, Asn 996, Leu 718, Pro 794, Leu 792, Ile 715, Lys 728, Tyr 998, Arg 999, Lys 716, Val 728, Ala 743, Gln 791, Leu 844, Met 793, Gly 796, Cys 797, Asp 800, Gly 3733, Val 726, and Leu 792.

In the 3D structure of the protein−ligand complex, it was observed that saroglitazar was binding at the same binding pocket as the native ligand. Figure 6A,B depicts the amino acid residues near 4 Å of the ligand.

Saroglitazar formed a complex with EGFR through conventional and nonconventional H-bonds. The residues that had interactions with the ligand through conventional H-bonds are Lys 728, Tyr 998, Arg 999, Asn 996, and Phe 997. The common amino acid residue in the active site of the receptor that forms conventional H-bonds with the atoms of saroglitazar and lapatinib is LYS 728 (see Figure 6C,D). The complex had nonconventional H-bond interactions. A total number of 686 nonconventional H-bonds were identified in the model, out of which 104 (15.16%) interactions were identified with saroglitazar. The interacting residues that formed nonconventional hydrogen bonds with saroglitazar are mentioned in the supplementary file. Saroglitazar had a binding affinity of −7 kcal/mol, whereas its redocked native ligand had −8.5 kcal/mol. These findings suggest that saroglitazar binds to EGFR but is less potent than lapatinib.

2.10. Molecular Dynamic Simulations. *2.10.1. RMSD and RMSF Calculations.* Within 10 ns and 100 ns simulation intervals, the RMSD variation was within 2−3 Å. The average RMSD values for the protein EGFR-saroglitazar complex was 2.99 Å and presented deviations until 2.29 ns, followed by an equilibrium throughout the 10 ns simulation (see Figure 7A). The average RMSD values of EGFR in its apo and holo states were 1.79 and 1.75 Å, respectively, and no significant changes in the RMSD values were observed after ligand binding (see Figure 7 B). The average RMSD values for the protein EGFR-saroglitazar complex throughout 100 ns intervals were lower than 10 ns simulation, i.e., 1.26 Å. The complex presented deviations on 30 ns, followed by stable RMSD values until remaining 100 ns (see Figure 7C,D).

The flexibility of the complexes was analyzed as saroglitazar was present in the active pocket of EGFR. The considerable RMSD values in the protein structure and ligands were supported by acceptable RMSF values for residues of proteins (3.5 Å) and atoms in the ligands (2.38 Å) respectively, during the MD simulation (see Figure 7E) throughout 10 ns interval. In 100 ns interval, the RMSF values for proteins is fluctuated high at 5.3 Å in the end, while remaining α helix and beta strands were much more rigid and fluctuated less than the unstructured part of the protein. The RMSF for atoms of the ligands was in the range of 0.66−2.23 Å in 100 ns simulation. The average RMSF values in the residues of the protein for the C-alpha was 1.09 Å and that for the backbone was 1.11 Å. The average ligand RMSF values with respect to protein was 0.967 Å. These values are acceptable RMSF range.

2.10.2. Protein Secondary Structure Elements (SSEs). The SSE composition analysis and SSEs distribution of the residue index of EGFR are illustrated in the supplementary file (see Figure S2). The EGFR-saroglitazar complex had 42% of total secondary structure, with 30.90% of an α helix and 11.51% of beta strands. The total secondary structure of EGFR alone was

https://doi.org/10.1021/acsomega.2c07570
ACS Omega 2023, 8, 14985−15002

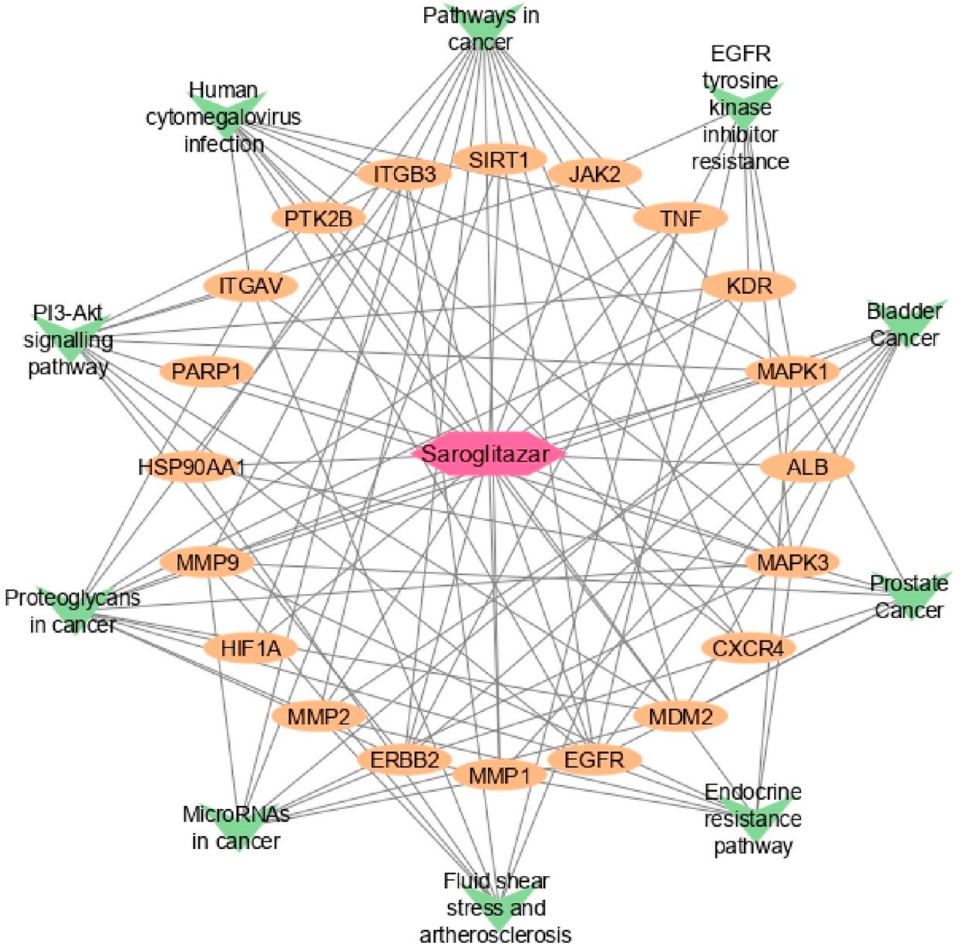

Figure 5. Compound−target−pathway network.

Table 2. Docking Scores and Clustering Coefficient of Various Putative Targets with Saroglitazar

name	clustering coefficient	Schrödinger score affinity (kcal/mol)	autodock-4 affinity (kcal/mol^2)
ERBB2	0.34	−10.538	−8.18
KDR	0.4	−9.67	−9.11
EGFR	0.27	−8.79	−7.79
MAPK1	0.21	−7.867	−7.18
JAK2	0.21	−7.135	−6.9
TNF	0.34	−6.215	−6.45
PARP1	0.51	−6.194	−8.99
CXCR4	0.36	−6.121	−8.95
HIF1A	0.26	−5.974	−8.71
MAPK3	0.24	−5.493	−7.62
MMP9	0.29	−5.344	−8.71
ITGB3	0.51	−5.303	−8.42
ITGAV	0.39	−5.303	−8.42
PTK2B	0.53	−5.225	−5.91
HSP90AA1	0.17	−4.978	−6.28
SIRT1	0.4	−4.786	−8.22
MMP2	0.45	−4.557	−7.94
MDM2	0.25	−4.471	−5.54
MMP1	0.4	−2.902	−5.89
ALB	0.24	−6.03	−10.16

46.25%, with 33.27% alpha helices and 12.98% beta strands. After 100 ns MD simulation the EGFR-saroglitazar complex had 41.42% of total secondary structure, with 29.49% of an α helix and 11.93% of beta strands.

2.10.3. Rotatable Bonds. For the prediction of the rotatable bonds of saroglitazar, it is necessary to identify the torison angles. The relationship between the torison angle present in the saroglitazar and its corresponding potential energy was exhibited by torison plots (see Figure S3). When saroglitazar was complexed with EGFR, it revealed 10 rotatable bonds. The histogram and torison of potential relationships provide insights into the conformational strain the ligand undergoes to maintain a protein-bound conformation. The ligand modification illustrated in the Figure S4 includes RMSD, radius of gyration, intramolecular hydrogen bonds, molecular surface area (MolSA), solvent accessible surface area (SASA), and polar surface area (PSA).

2.10.4. Protein−Ligand Contacts. The images in Figure 8A,B present the 2D summary of the interaction analysis results of saroglitazar with EGFR. These interactions occurred with a probability of over 23% during simulation. In-depth intermolecular interactions were analyzed. There were about 0−9 contacts found between saroglitazar and EGFR. Saroglitazar formed hydrophobic bonds with EGFR from Leu 718 to Met 766, Leu 777 to Leu 844, and Leu 858 to Met 1002. Hydrogen bond interactions were observed between saroglitazar and Cys 775, Arg 776, Asp 855, and Phe 856. The H-bond interaction was formed with more than 70% probability of the simulation time with Cys 775 and Asp 855 (see Figure 8A−D). After 100 ns of simulation, H bonds with

https://doi.org/10.1021/acsomega.2c07570
ACS Omega 2023, 8, 14985−15002

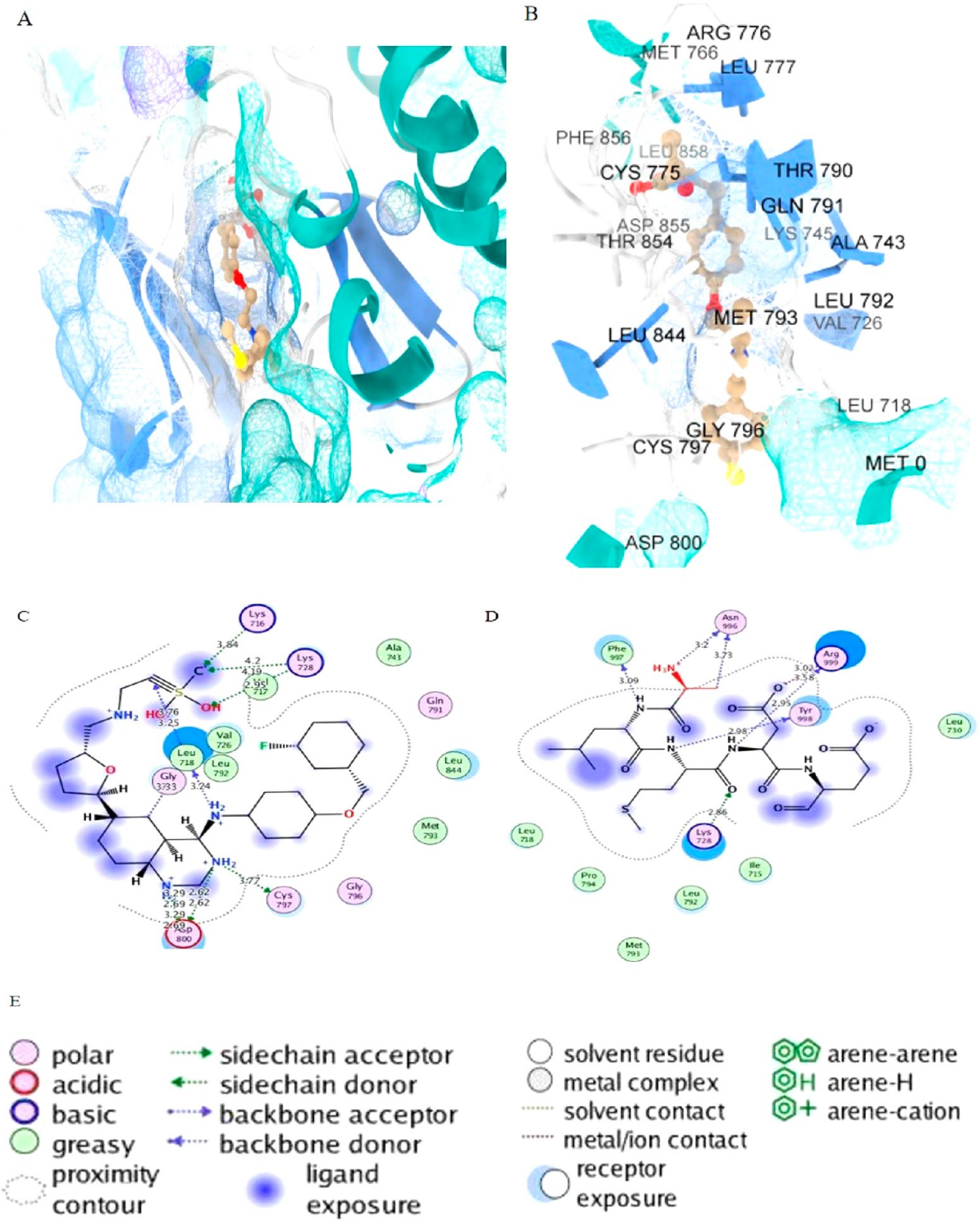

Figure 6. A: 3D structure of saroglitazar bound with EGFR. B: Zoomed image of the protein−ligand complex along with amino acid residues within a distance of 4 Å from the ligand. C: 2D interaction diagram of a native ligand (lapatinib) with EGFR. D: 2D interaction diagram of saroglitazar with EGFR. E: Index that illustrates different hydrogen bonds.

ASP 885 was formed in more than 100% probability of the simulation time. In 100 ns simulation, saroglitazar interacted with hydrogen bonding, hydrophobic bonding and water bridges with Lys 745. Hydrogen bonds were formed with Lys 745, Thr 854, and Asp 855 (see Figure 8 A−D).

2.11. Saroglitazar Administration Inhibited Blood Vessels in the CAMs. Saroglitazar administration at a dose of 0.06 $\mu g/\mu L$ inhibited the vascular area by 38.30%. The percentages of inhibition for the vessel area after 0.2 and 2 $\mu g/\mu L$ saroglitazar were 56.46% and 68.59%, respectively (see Figure 9). The average vessel area is presented in Figure 9.

2.12. EGFR Expression in CAM Assay. Section examined after saline administration showed moderate cytoplasmic positivity of IHC EGFR in the endothelial cells of blood

https://doi.org/10.1021/acsomega.2c07570
ACS Omega 2023, 8, 14985−15002

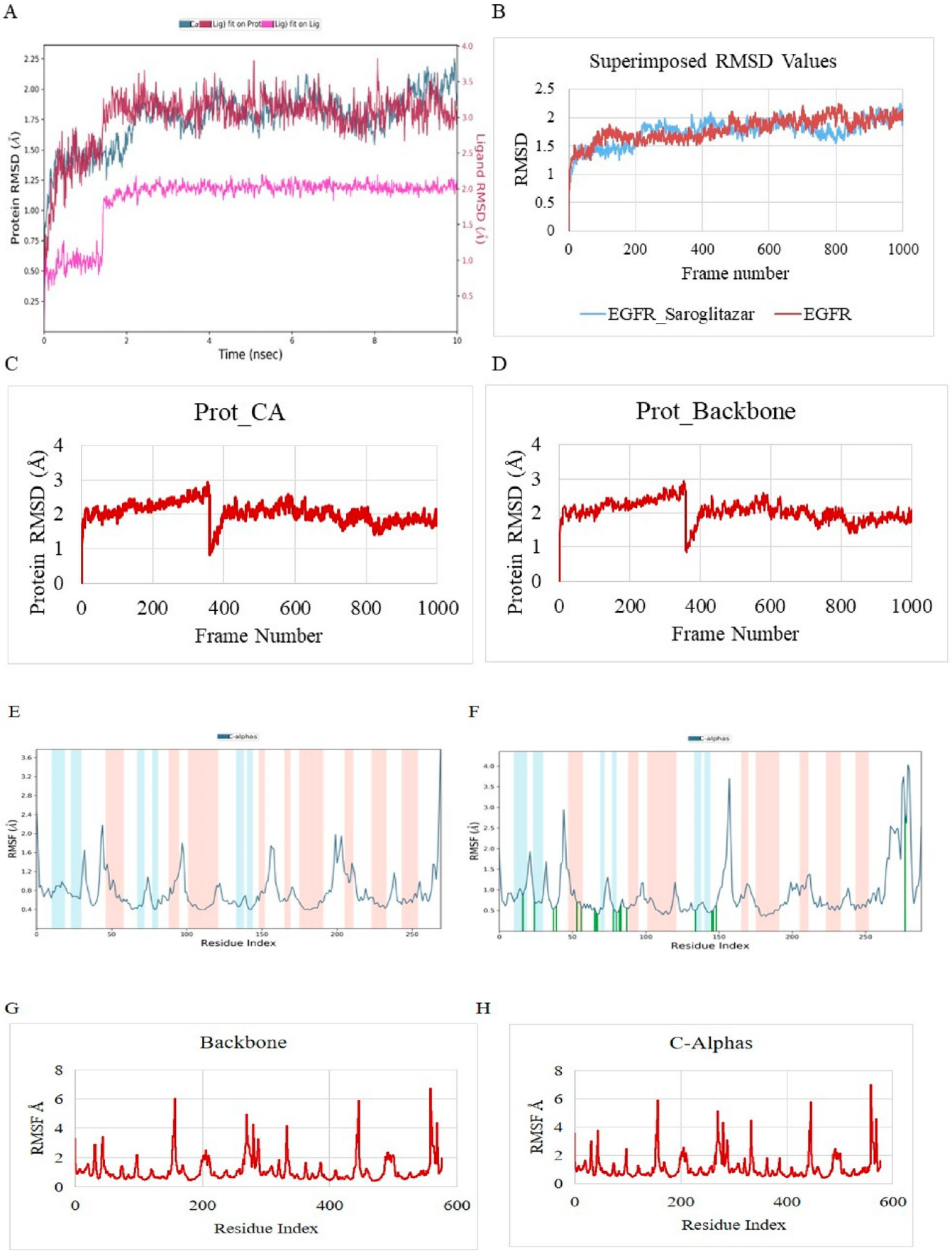

Figure 7. A: RMSD plots of the EGFR-Saroglitazar complex. B: Superimposed RMSD values of EGFR in its apo and holo states, 1 ns = 100 frames. C: C-alpha RMSD values of saroglitazar-EGFR complex during 100 ns interval; 1 ns = 10 frame number. D: Backbone RMSD values of saroglitazar-

https://doi.org/10.1021/acsomega.2c07570
ACS Omega 2023, 8, 14985−15002

Figure 7. continued

EGFR complex during 100 ns interval, 1 ns = 10 frames. E: RMSF plots of the EGFR alone during the 10 ns MD simulation period. F: RMSF plots of the EGFR-saroglitazar complex during the 10 ns MD simulation period. G: Backbone RMSF plots of the EGFR during the 100 ns MD simulation period. H: RMSF plots of the C-alphas EGFR-saroglitazar complex during the 100 ns MD simulation period. The α helix and beta strand regions are highlighted in red and blue backgrounds, respectively. Protein residues that interact with the ligand are marked with green-colored vertical bars.

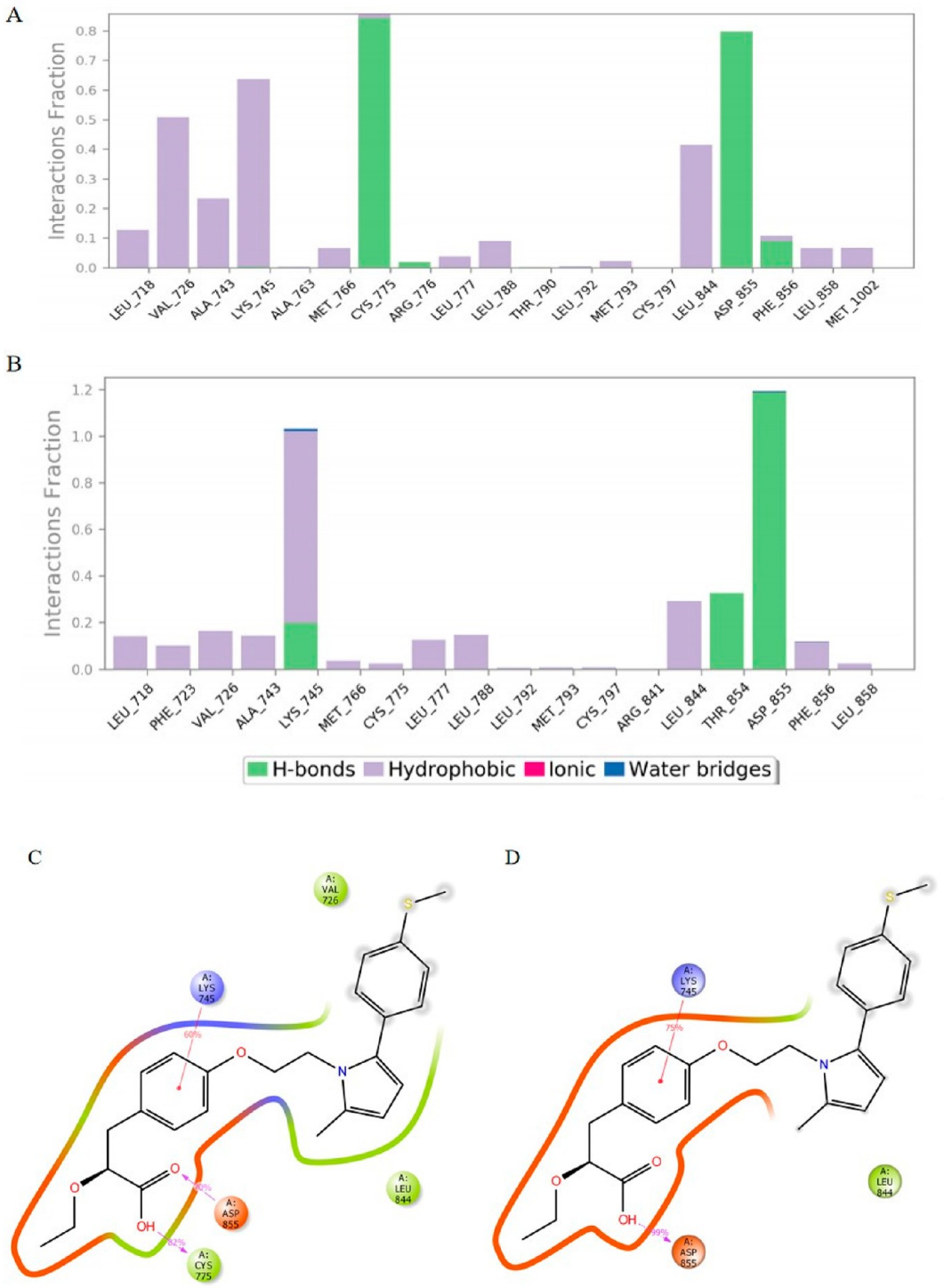

Figure 8. A: EGFR-Saroglitazar contacts after 10 ns simulation. B: EGFR-Saroglitazar contacts after 100 ns simulation. C: EGFR-Saroglitazar contact summary after 10 ns simulation. D: EGFR-Saroglitazar contact summary after 100 ns simulation.

vessels. Nonspecific positivity by cubodial epithelium is seen. The connective tissue layer contains many blood vessels lined by endothelial cells with focal proliferation. Few of the endothelial cells are proliferating and migrating. The section

https://doi.org/10.1021/acsomega.2c07570
ACS Omega 2023, 8, 14985−15002

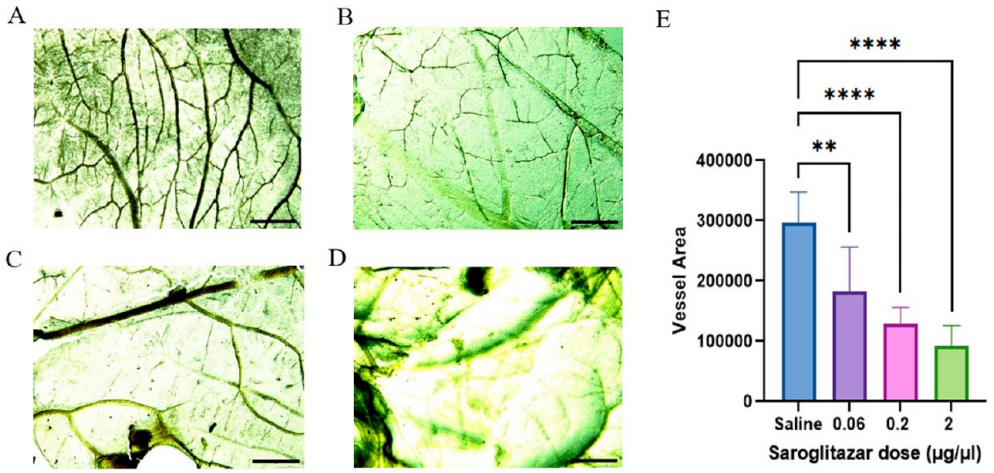

Figure 9. Figure represents the stereoscopic images of the CAM membranes treated with A: saline, B: saroglitazar 0.06 μg/μL, C: saroglitazar 0.2 μg/μL, D: saroglitazar 2 μg/μL. Magnification: 1.5×; scale: 200 μm. E: Vessel area after saroglitazar exposure $n = 6$, $^{**}p < 0.0021$, $^{****}p < 0.0001$.

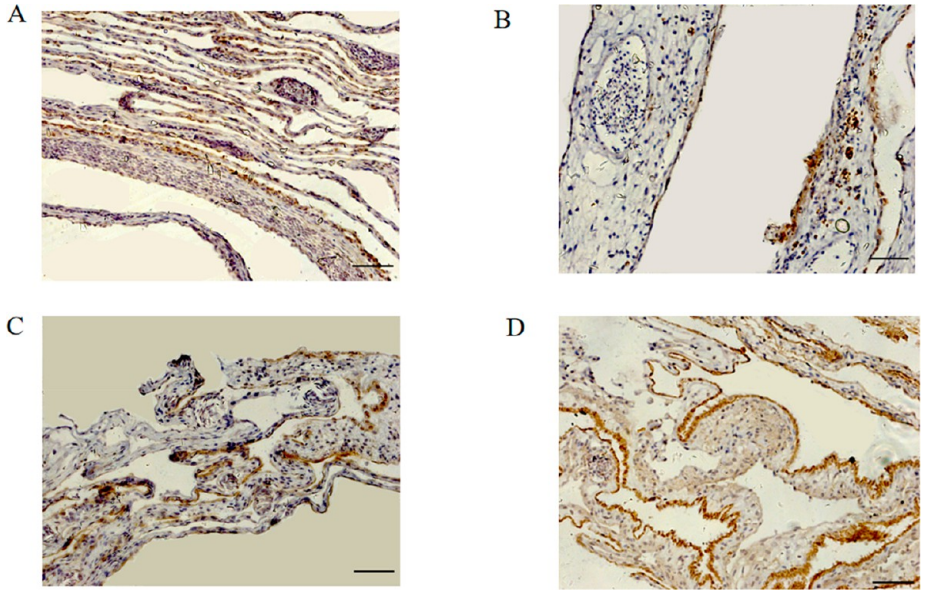

Figure 10. Figure represents the EGFR expression in CAM membranes treated with A: saline, B: saroglitazar 0.06 μg/μL, C: saroglitazar 0.2 μg/μL, D: saroglitazar 2 μg/μL. Magnification: 20×; scale: 50 μm.

treated with 0.06 μg/μL saroglitazar demonstrated scattered moderate cytoplasmic positivity of IHC EGFR in the endothelial cells of blood vessels in connective tissue layer. Nonspecific positivity by cubodial epithelium is seen. Connective tissue layer contains few scattered blood vessels lined by endothelial cells with focal proliferation along with scattered inflammatory cells. Very few endothelial cell migration was observed. After 0.2 μg/μL saroglitazar administration, the section examined shows scattered weak cytoplasmic positivity of IHC EGFR in the few scattered endothelial cells of blood vessels in connective tissue layer. No endothelial migration or proliferation seen. Nonspecific positivity by cubodial epithelium is seen. Connective tissue layer contains few scattered blood vessels lined by endothelial cells. After 2 μg/μL saroglitazar administration, the section examined shows negative expression of immunohistochemistry EGFR in the connective tissue layer of membrane. Nonspecific positivity by cubodial epithelium is seen. Connective tissue layer contains very few scattered blood vessels lined by endothelial cells. Endothelial cell proliferation and migration are not observed (see Figure 10).

3. DISCUSSION

The current study examines the effect of saroglitazar on angiogenesis. This is followed by the identification of targets predicted to interact with saroglitazar and influence angiogenesis. Consequently, the pathways through which saroglitazar may function and modulate angiogenesis were discovered and examined to provide a systematic explanation of the mechanism of action of the drug.

Saroglitazar is used to treat diabetic dyslipidemia. The current study demonstrated that saroglitazar had a potent inhibitory effect on blood vessel formation. The chicken CAM assay is an established paradigm for the screening of angiogenesis modulators. Bevacizumab, sunitinib, thalidomide, and other therapeutically licensed antiangiogenic drugs inhibited angiogenesis in the CAM membrane of chicken embryos.[23,24] In addition, drugs with antiangiogenic activity in

https://doi.org/10.1021/acsomega.2c07570
ACS Omega 2023, 8, 14985−15002

the CAM assay have demonstrated anticancer potential in clinical studies.[25] Given the advantages over traditional *in vitro* and *in vivo* research models, the *in ovo* research paradigm was used in the current study to assess the angiogenesis modulating effect of saroglitazar. Using *in ovo* testing, we observed that this drug strongly inhibits angiogenesis, providing evidence for its preventative and therapeutic actions on angiogenesis-related comorbidities in diabetic patients, such as retinopathy, nephropathy, neuropathy, and arterial atherosclerosis. However, the precise target through which this drug suppresses angiogenesis to produce these effects remains to be unraveled.

Computer inference methods are used to predict the targets of specific inhibitors, reposition drugs, and explain off-target interactions.[26] The target identification method revealed that saroglitazar interacts with 104 angiogenesis-related target genes. The degree exponent of the current network indicates the presence of hubs.[27,28] The path length and clustering coefficient of the network were minimal, indicating that the nodes of the network transmit information rapidly. However, because the network has fewer connections, it has a greater probability of binding the drug or another ligand.[22] This network analysis revealed that 20 hub targets were typically identified in both topological analysis and network clusters. Using centrality and modular analysis, these targets were determined to be pivotal for the angiogenesis-inhibiting activity of saroglitazar. This demonstrated that saroglitazar modulates angiogenesis not only through altering PPAR-alpha and PPAR-gamma but also via a complex network of interconnected pathways. Following the examination of pathways, it was determined that the majority of hub genes were involved in pathways in cancer, proteoglycans in cancer, and the PI3K-Akt signaling pathway. Numerous angiogenesis-related targets, including VEGF, angiopetins, and nitric oxide, are regulated by the PI3K-Akt signaling pathway. This pathway inhibition has resulted in a decrease in VEGF and angiogenesis.[29] This shows that saroglitazar may regulate the PI3-Akt signaling pathway and other cancer-related processes. In this study, HSP90AA1 was identified as the hub gene and was found to influence four of the ten most important pathways. HSP90AA1 is overexpressed in a variety of malignancies, including bladder cancer and leukemia, and is necessary for the survival of tumor cells; its inhibition increases the sensitivity of tumor cells to chemotherapy.[30] HSP90AA1 is an EGFR client protein. It stabilizes EGFR, and their connection is vital to the survival of malignancies dependent on EGFR. Moreover, HSP90AA1 controls cancer via the EGFR signaling pathway. Its inhibition causes a decrease in EGFR, demonstrating the interdependence of these two targets.[31,32] Through this research, a comprehensive list of targets was obtained; nevertheless, molecular docking was performed to predict the preferred target with the highest binding affinity for saroglitazar when it is present in the vicinity of a cell.

According to docking studies, ERBB2, KDR (VEGFR2), and EGFR were identified to have the highest binding affinities with saroglitazar. In one study, saroglitazar dramatically decreased VEGFR2 levels in diabetic rats, confirming our *in-silico* results demonstrating interaction between saroglitazar and KDR (VEGFR2).[8] There is no publicly accessible data about the effect of saroglitazar on ERBB2 and EGFR. EGFR is a protein tyrosine kinase and functions via the protein tyrosine PI3-AKT signaling pathway, which leads to endothelial cell proliferation, migration, and angiogenesis. The over-representation of these pathways is observed in various types of cancer. Following the analysis of the current study, topological analysis identified EGFR as a hub target. Following the functional enrichment analysis, a consistent enrichment of biological processes and pathways associated with EGFR were observed. The analysis showed enrichment of interconnected signaling events and highlighted biological processes like enzyme-linked protein signaling pathway, transmembrane receptor protein tyrosine kinase signaling pathway, positive regulation of cell population proliferation, and positive regulation of cell migration. In pathway enrichment analysis, the EGFR tyrosine kinase inhibitor resistance, PI3-Akt-signaling pathway, pathways in cancer and bladder cancer were enriched. All together, these findings highlight that saroglitazar may interact with EGFR and inhibit the PI3-AKT signaling pathway and may impede endothelial cell proliferation, migration, angiogenesis, and further angiogenesis-associated diseases (Figure 4). Additionally, for the final target screening, targets with the highest binding energies, the lowest cluster coefficient, and the greatest pathway coverage were chosen. The best docking scores were used to refine the targets because they are a technique for determining whether thermodynamic interaction between the target and ligand is possible. This was followed by screening a target with a comparatively lower clustering coefficient, since it indicates that the node is not densely packed with other proteins and has space for interacting with other ligands.[22] EGFR had the highest binding affinity and was engaged in nine of the top ten enriched pathways with the lowest clustering coefficient. Furthermore, it is upregulated in the diabetic population. Finally, EGFR was identified as the refined target with the highest docking scores, significant upregulation in diabetics, the greatest number of associated pathways, and the lowest clustering coefficient values, making it the most important and druggable target. Drug-ligand interaction analysis and molecular dynamics simulations were performed on the EGFR structure, which was determined to be the optimal target. Lapatinib is an EGFR tyrosine kinase inhibitor, and competes with the ATP binding site of EGFR to abrogate its phosphorylation and signal transduction.[33] In the current study, the crystal structure of EGFR bound to lapatinib was utilized for docking studies. Thus, for protein−ligand interaction analysis, lapatinib was used as a reference to determine the activity of saroglitazar. Saroglitazar was bound to the same active site of EGFR as lapatinib. The binding affinity of saroglitazar with EGFR was good but slightly less potent than lapatinib. saroglitazar, and laptininb both formed hydrogen bonds with Lys 728 in the ATP-binding site of the EGFR. In previous bioinformatic studies 2-*O*-caffeoyl tartaric acid and 2-*O*-feruloyl tartaric acid blocked the ATP binding site of EGFR tyrosine kinase located from Leu718−Val726 and formed hydrogen boinds with Lys728, which is a key residue of EGFR.[34] Afatinib, another inhibitor of EGFR tyrosine kinase activity, showed binding interaction with Lys 728.[35] These studies supports that saroglitazar interacts with one of the crucial amino acid of EGFR. Apart from Lys 728, saroglitazar interacted with another significant amino acid of EGFR, i.e., Tyr 998. Amino acid Tyr 998 is phosphorylation site of EGFR.[36] The findings from the study conducted by Tong et al. implied that EGF receptor trafficking is governed by the coordinated phosphorylation of EGFR at sites Tyr 998, Ser 991, Ser 1039, and Thr 1041[37] indicating that amino acid Tyr 998 is crucial for the signal transduction of EGFR, and that the interaction of saroglitazar with this amino acid may hamper the phosphorylation at this site. These results reflected that

https://doi.org/10.1021/acsomega.2c07570
ACS Omega 2023, 8, 14985−15002

Table 3. RMSF Values of the Key Residues Detected from Protein−Ligand Interaction

	RMSF							
residue number	Val_726	Ala_743	Lys_745	Cys_775	Cys_797	Asp_855	Leu_844	Thr_854
10 ns	0.723	0.524	0.621	0.570	0.563	0.497	0.508	0.455
100 ns	0.768	0.561	0.635	0.511	0.633	0.526	0.554	0.500

saroglitazar can also compete for the ATP binding site and consequently antagonize EGFR. These data were supported by molecular dynamics simulations. The simulation revealed that the EGFR interacts with saroglitazar in a steady manner. During the MD simulation, the backbone deviation (N, Cα, C) of protein was computed using the RMSD value. The complex structures were initially a little unstable (2 Å) until equilibrium was reached. After 2 ns of equilibration, the system stabilized, and this trend continued for the next 10 ns. The RMSD of the complexes varied between ∼1.75 and ∼2.25 Å after 2 ns. Notably, the RMSD of the saroglitazar-EGFR complex was minimal in simulations lasting for both 10 and 100 ns, fluctuating by no more than 2−3 Å, and the molecules were extremely stable. These results suggested that the structure of EGFR bound to saroglitazar did not undergo any significant structural changes during the MD simulation. The RMSD analyses demonstrate that saroglitazar and EGFR exhibited structural stability throughout the MD simulation. In addition, the flexibility of the complexes and the ligands present in the active site of the protein were examined. The RMSF values were obtained to assess the fluctuation of the complex as a function of time. In 10 and 100 ns simulation intervals, the complex exhibited minimal fluctuations. The C-terminus shows higher fluctuation (∼4 Å after 10 ns and ∼7 Å after 100 ns simulation) than the N-terminus (∼2 Å after 10 ns of simulation interval and ∼3.7 Å after 100 ns of simulation interval). Due to strong intermolecular contact with the protein, saroglitazar was extremely stable in its catalytic region. Due to the intermolecular interactions between ligand molecules and protein, the complex displayed modest fluctuations. The protein molecule was slightly rigid due to these intermolecular interactions and secondary structural elements (alpha helices and beta strands). These results presented the presence of saroglitazar at an active pocket of EGFR and during the simulation period. Therefore, in accordance with the molecular docking results, the RMSD and RMSF values supported the formation of stable complex between saroglitazar and EGFR. After analyzing the secondary structure of unbound EGFR, it was determined that the protein possessed secondary structures at both its N- and C-termini. The protein's N-terminus possesses beta strands, while the C-terminus contained α helix, demonstrating EGFR as extremely helical. After SSE analysis, it was found that the binding of saroglitazar with EGFR decreased the α helix of the protein at the C-terminus in both 10 ns and 100 ns simulations. Additionally, the α helix from the central region of the protein decreased following ligand interaction, however, no alteration was found in the beta strands after ligand binding. These alterations in the secondary structures were evident after both 10 and 100 ns simulations (see Supporting Information 1, Figure S2). This stated that, similar to the unbound protein, the complex was quite helical. After 100 ns of the MD simulation, mild changes in the structure of the α helix were observed, stating that no significant changes in the secondary structure of the protein were observed after saroglitazar binding to EGFR. The radius of gyration (rGyr) is a major measure of the folding state of a protein under various situations. During this study, the rGyr of the saroglitazar-EGFR complex was evaluated to gain insight into the compactness of the protein. After 10 and 100 ns of simulation, the rGyr of the saroglitazar-EGFR complex fluctuated between 4.88−5.98 and 4.9−5.71 Å, respectively. The average values for rGyr were 5.61 and 5.27 Å during a 10 and 100 ns simulation times, respectively. During the simulation period, the different surface areas of EGFR in complex with saroglitazar such as molecular surface area (MolSA), solvent accessible surface area (SASA), and polar surface area (PSA) were evaluated to determine the confirmational stability of the EGFR-Saroglitazar complex. MolSA, SASA, and PSA of EGFR were in the range of 416 Å^2-448 Å^2, 10 Å2−125 Å^2 and 88 Å2−120 Å^2 respectively, after 10 ns of the simulation interval. However, after 100 ns simulations, the MolSA, SASA, and PSA of EGFR were in the range of 416.94−441.56 Å^2, 24.58−169.226 Å^2, and 77.92−114.054 Å^2, respectively, depicting the intactness of the complex. The observations from EGFR-saroglitazar contacts after 10 and 100 ns MD simulations suggested significant intermolecular protein−ligand interactions (hydrogen bonding, hydrophobic bonding, and water bridges). In accordance with the graphs in Figure 8A,B, the hydrogen bond (H-bond) and hydrophobic interaction accounted for the majority of the interaction between EGFR and saroglitazar. Nevertheless, the H-bond interaction between saroglitazar and two amino acid residues, namely, Asp_855 and Cys_775, appeared to be highly significant. Analysis of the RMSF values of the key residues, identified through protein−ligand interactions, can be utilized to evaluate structural movement and flexibility. Since the binding site of the protein is mostly comprised of several crucial residues, in the present study eight critical residues consisting of Val_726, Ala_743, Lys_745, Cys_775, Cys_797, Asp_855, Leu_844, and Thr_854 were chosen for RMSF calculation. The summary of the data is presented in Table 3.

The change in RMSF values of selected eight residues for EGFR protein was observed to be in lockstep. This demonstrated that these residues can move as a cohesive unit. The statistically most flexible residue was Val_726 with a high RMSF value, whereas Asp_855 and Thr_854 were the most stable residues with a moderate RMSF value. Residue Lys_745 was connected through both, hydrophobic and polar bonds. The seven remaining residues out of the eight screened residues can be divided into two categories: hydrophobic residues (726, 743, 745, 844) and polar residues (775, 854, 855). According to this analysis, it was concluded that the critical residues of EGFR responded to saroglitazar via two fundamental interactions (hydrogen bond and hydrophobic interactions). Asp_800, Met_793, Leu_844, and Ala_743 were found as important residues for the EGFR Kinase domain in a recent study.[38] In the current study, effective interactions of saroglitazar with these residues were observed, stating that saroglitazar can potentially interact with the key residues of EGFR and significantly affect its function.

Overall, an efficacious interaction of saroglitazar with these residues was detected in the current investigation, indicating

https://doi.org/10.1021/acsomega.2c07570
ACS Omega 2023, 8, 14985−15002

that saroglitazar may interact with the critical residues of EGFR and impede its activity. The results identified EGFR as the strongest and most preferred target for saroglitazar in this interactome. The EGFR inhibitor geftininb inhibited the angiogenic process in the CAM membrane in a previous study, indicating the roles of EGFR expression and EGFR-mediated angiogenesis in the CAM.[39] Therefore, to simultaneously assess EGFR expression and its effect on the angiogenic process, IHC staining of CAMs was performed. In comparison to 2D cell culture models in which monolayer cell cultures are isolated systems and lack complex physiological conditions, the chicken embryo model is unique due to its accessible CAM membrane in which blood vessels grow in a three-dimensional framework, which is advantageous as it mimics the true biological complexities. This model eliminates the need for rodents in angiogenesis inhibitor screening, hence reducing or replacing the number of vertebrates in the study in accordance with the 3 R's of animal ethics. In the current investigation, the experiment was repeated by administering graded doses of saroglitazar, and stereoscopic examination of the blood vessels indicated that significant inhibition in the vessel area was observed in a dose-dependent manner. Increasing saroglitazar doses were also associated with a decrease in endothelial cell proliferation and migration, as observed in the IHC analysis of the CAMs. Additionally, EGFR expression in the endothelial cells decreased in a dose-dependent manner, but in the cuboidal epithelium, an increase in EGFR expression was observed. The pathological findings also represented a substantial decrease in blood vessel density, indicating that saroglitazar inhibits EGFR-mediated angiogenesis. The enhanced EGFR expression in the epithelium following treatment with saroglitazar may result from the homeostasis mechanism of CAM compensating for the inhibitory effect of saroglitazar on EGFR. In addition to the clinical complications associated with angiogenesis, critical proteins linked with enhanced angiogenesis, such as VEGFR 2 and EGFR, are elevated in diabetic patients. EGFR is upregulated in diabetic individuals, which contributes to numerous pathologies, including pancreatic fibrosis,[6] renal damage,[40−42] and vascular dysfunction.[43,44] In addition, the diabetic nephropathy model demonstrates upregulation of renal EGFR, and blocking this receptor protects against the development of diabetic nephropathy,[45] indicating that inhibition of EGFR-mediated angiogenesis is a target for the prophylaxis and treatment of EGFR-associated complications in diabetes. The inhibitory activity of saroglitazar on upregulated angiogenic markers like VEGFR2, as determined in prior studies,[8] and EGFR, as determined in the present study, suggests that future research can investigate the effects of saroglitazar on diabetic nephropathy, neuropathy, obesity, retinopathy, and other conditions associated with aberrant angiogenesis. A few studies have demonstrated an elevated cancer risk in diabetic individuals.[46−51] On the other hand, epidemiological studies have demonstrated a decreased incidence of cancer in patients administering metformin, a widely used antidiabetic medication.[52] Intriguingly, an epidemiological study of 6103 diabetic patients revealed that the antidiabetic medications gliclazide and glibenclamide may reduce the incidence of cancer in a dose-dependent manner with sustained usage. A preclinical investigation supported the efficacy of glipizide in cancer prevention by inhibiting angiogenesis.[53] These studies suggest that prolonged use of antidiabetic drugs with a secondary pharmacological target on angiogenesis can prevent certain malignancies in the diabetic population. In the current investigation, the CAM was exposed to saroglitazar for 48 h, from embryonic development day (EDD) 7 to EDD 9, which, according to our preliminary study, is the optimal treatment window for analyzing the effect of medicines on rapidly developing blood vessels in the CAM. As the results of the enrichment analysis in this study identified cancer-related pathways in the action of saroglitazar, we hypothesized that the drug could be effective in inhibiting cancer progression where blood vessel development is rapid by inhibiting EGFR-mediated angiogenesis and endothelial cell proliferation (Figure 4). According to this study, long-term use of saroglitazar may reduce cancer risks by angiogenesis suppression and EGFR antagonism in the diabetic population, which suggests that more research is needed in this area. Moreover, since angiogenesis plays a critical role in physiological processes like wound healing and embryonic development, inhibiting this process may result in abnormalities of these functions. In order to determine the usefulness and contraindications of the medications, however, a risk−benefit analysis must be conducted. An example of this is the drug thalidomide, which suppresses angiogenesis and has been repurposed as a cancer treatment but historically has caused devastating birth defects. These defects are due to oxidative stress induction and angiogenesis inhibition.[54] Antiangiogenic medicines are teratogenic, and angiogenesis suppression is a potential cause of embryotoxicity.[55] These studies, along with the current research warrant further research on the teratogenic potential of saroglitazar since it inhibits angiogenesis. By conducting these trials, we could gain a better understanding of how saroglitazar compares in terms of the proposed risks and benefits, which are not yet reflected in the scientific literature.

4. CONCLUSION

In the current investigation, it was discovered that saroglitazar had antiangiogenic potential. Moreover, saroglitazar-rewired biomolecular components were illustrated via system biology tools. No reports have revealed the topological network and key regulatory targets of saroglitazar that govern angiogenesis-related pathways. This article describes the ongoing research and development process that led to the construction of a potential PIN. The key targets for initiating and regulating the pharmacological actions of saroglitazar on angiogenesis have been identified. Using docking scores, topological analysis, and pathway enrichment analysis, EGFR was the most robust regulatory protein. The molecular dynamic simulations revealed a stable complex and modest structural alterations in EGFR after saroglitazar binding, indicating a steady protein−ligand binding without alteration in the rigidity of EGFR. Strong interactions between saroglitazar and EGFR in a 10 ns simulation period corroborated this conclusion. The IHC expression of EGFR in the CAM epithelium was upregulated in a dose-dependent manner. Despite the EGFR overexpression, there was a significant decrease in endothelial cell proliferation, migration, and blood vessel density. The positive correlation between EGFR expression in endothelial cells and angiogenesis followed by negative correlation between EGFR expression in the CAM epithelium and the angiogenic process after saroglitazar exposure in escalating doses in the CAM membrane is evident proof that the drug reduces angiogenesis by interacting with EGFR. In conclusion, the current study provided an effective alternative preclinical

https://doi.org/10.1021/acsomega.2c07570
ACS Omega 2023, 8, 14985−15002

paradigm for exploring the mechanistic insights of saroglitazar against angiogenesis and offered innovative research opportunities in diabetic complications and in the drug development process (see graphical abstract). This study also suggests the need for future research to investigate the effect of this medicine on tumors, tumor-mediated angiogenesis, and teratogenic potential.

5. MATERIALS AND METHODS

5.1. Chicken CAM Assay. *5.1.1. Handling of the Chick Embryos.* The tests conducted on the chicken embryo did not require approval from the animal ethics committee; hence, no administrative processes were followed.[56] The fertilized white leghorn eggs were obtained from Keggfarm in Gurugram, Haryana. The eggs were properly washed with an antimicrobial rinse, blotted, and placed with the blunt end up in a humidified egg incubator. The eggs were kept in the incubator until the seventh day of incubation. On day 7, a window was created on the egg for the drug delivery. The eggs were then sealed using a parafilm. The eggs were kept back in the incubator for the next 48 hours.

5.1.2. Study Design and Experimental Protocol. The CAMs of growing chicken embryos were exposed to escalating dosages of saroglitazar. The doses were selected on the basis of preliminary dose escalation studies. The preliminary dose escalation tests were conducted at concentrations of 0.06, 0.2, 0.6, 2, and 4 μg/μL when determining the optimal dose. Since, mortality was observed in 4 μg/μL, data in this dose was eliminated from the studies, and 3 dose levels were selected for further experiments. Each of the four study groups contained five viable embryos. The following study groups were included: Vehicle controls include solvent administration, and the treatment groups were 0.06 μg/μL saroglitazar, 0.2 μg/μL saroglitazar, and 2 μg/μL saroglitazar. After drug exposure, the embryos were sealed with tape and cultured for another 48 h. The incubation was followed by regular assessments of viability until the ninth day of gestation. On day 9 of gestation embryos were euthanized using hypothermia, and the CAM vasculature were photographed using a digital camera for future examination. Only viable embryos were used for the analysis. The evaluation method is explained in Evaluation of Angiogenesis.

5.1.3. Evaluation of Angiogenesis. The macroscopic images of the treated CAMs were evaluated for scoring by two blinded graders. The scoring was based on methodologies proposed in prior research.[57] CAM membranes with unchanged blood vessels were given a score of 0. Eggs with a small capillary-free area below the area of treatment, the presence of a few microcapillaries, or a minor reduction in the formation of blood vessels were graded as 1. Eggs with a capillary-free area beneath the area of treatment, no apparent microvessels, and massive vessels merging received a score of 2.

An average score of <0.5 was classified as having no antiangiogenic effect. An average score of ≥0.5 and ≤1 presented a weak antiangiogenic effect. An average score of >1 and <1.5 was considered good antiangiogenic effect and ≥1.5 was considered as strong antiangiogenic effect.

5.2. Screening the Putative Targets of Saroglitazar. The corresponding putative targets of saroglitazar were predicted by the spatial conformation of the collected compounds from the Swiss Target Prediction Tools at the Swiss Institute of Bioinformatics (SwissTargetPrediction, http://www.swisstargetprediction.ch/).[58,59] Target fishing was also done by performing inverse docking using the ACID server (http://chemyang.ccnu.edu.cn/ccb/server/ACID). The targets with a dock score between −8 and −11.5 were selected as saroglitazar targets from the ACID Inverse Docking Server.

5.3. Collection of Target Proteins Associated with Angiogenesis. We text-mined the Therapeutic Target Database (TTD, db.idrblab.net),[60] the Drugbank database (Drugbank, https://go.drugbank.com),[61] and a database of gene-disease associations, DisGeNET (http://www.disgenet.org/),[62] to search for angiogenesis-related targets. The gene names were retrieved from the Universal Protein Database (UniProt, https://www.UniProt.org/).[63]

5.4. Constructing and Visualizing a Protein−Protein Interaction Network (PIN). A Venn diagram was constructed to show the number of targets obtained from saroglitazar and angiogenesis. Using ugent.be,[64] the shared targets between saroglitazar and angiogenesis were hypothesized to be possible therapeutic targets for angiogenesis-associated disorders. The targets in the overlapped region were then analyzed with the STRING database[65] to generate a protein−protein interaction (PPI) network. PPIs with confidence ranges >0.7 for data scores were included in this study. Subsequently, the target network was constructed using Cytoscape 3.6.1.

5.5. Topological Analysis of the PIN. Topological properties of the network are crucial for gaining insights into complex networks. The PIN was analyzed using Cytoscape and its in-built plugin Network Analyzer for the calculation of basic topological parameters of saroglitazar-rewired PINs, including degree and closeness centrality. In the network, genes represent nodes, and the edges represent the interactions between nodes. The degree indicates the number of edges linked to the nodes. The highest degree of nodes represents significant biological function. Closeness centrality indicates how close a node is to all other nodes in the network.

5.6. Modular Analysis of PIN. The term "modulation" in this context means finding clusters (highly connected nodes or proteins) in the network. Clusters in the PPI network are protein complexes that are components of pathways. Cytoscape's MCODE plugin was utilized for PIN modulation.

5.7. Functional Enrichment Analysis. To explore the biological functions of saroglitazar acting on angiogenesis, the common targets screened via topological analysis and modularization were integrated for gene ontology (GO) and Kyoto Encyclopedia of Genes and Genomes (KEGG) enrichment analyses using the ShinyGO v0.76.2 database.[66] According to the GO database, the GO enrichment analysis includes studies of molecular function (MF), biological process (BP), and cellular component (CC). A KEGG enrichment study was conducted using the KEGG database.

5.8. Construction of a Compound−Target−Pathway Network. Through topological analysis (hub genes) and MCODE analysis (clusters), the highly connected genes in the PPI network were identified and used to construct the component−target network, incorporating the top 10 pathways from the KEGG enrichment study into the network. The relationships between these targets and the involved pathways were determined by constructing an integrated network with Cytoscape.

5.9. Molecular Docking Analysis. The objective of performing docking simulations was to predict the binding affinity of ligands and targets for known 3D structures. These

https://doi.org/10.1021/acsomega.2c07570
ACS Omega 2023, 8, 14985−15002

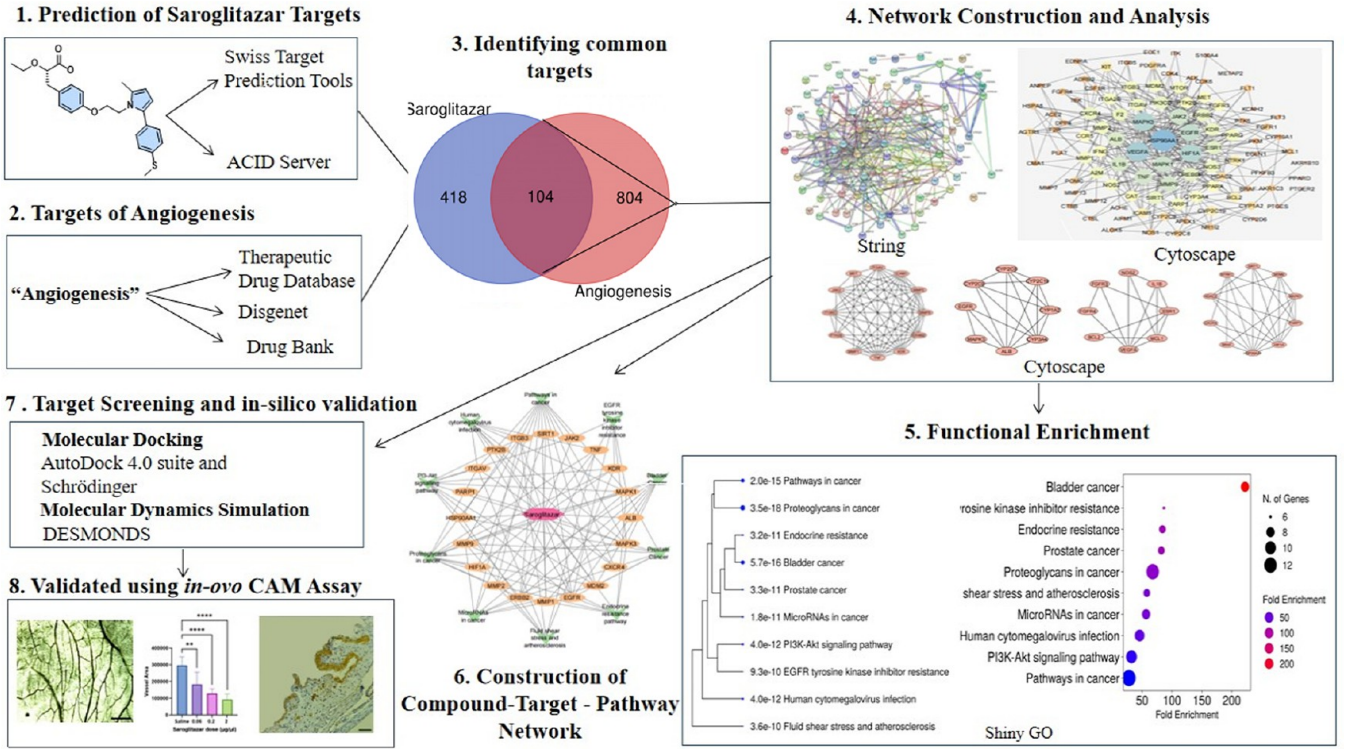

Figure 11. Methodology used in the current study.

simulations can validate the compound-target associations. The 3D structures of the key targets were downloaded from the RCSB PDB (http://www.rcsb.org/).[67] The PubChem (https://pubchem.ncbi.nlm.nih.gov/) database was used to retrieve the 3D structure of saroglitazar. The ligand was prepared by using Ligprep module and protein was prepared by using protein preparation wizard pluggins in the Schrödinger 2018 package. Finally, the study was performed using the AutoDock 4.0 suite, which revalidated the fashion of the score in the Glide module of the Schrödinger 2018 package for molecular docking verification. The binding energies were listed to evaluate the interaction between saroglitazar and targets. The binding energies less than −7.0 were considered filter criteria for assimilation of good binding interactions between saroglitazar and targets.

5.10. Molecular Dynamics Simulations. The molecular docking simulations were followed by molecular dynamic (MD) simulations using the Desmond package. MD simulations were performed to identify the effectiveness of saroglitazar against EGFR[68] and modulation using the SPC water model. All the systems were subjected to energy minimization, and the systems were placed in the cubic box with a buffered distance of 10 Å for the generation of a hydration model. Finally, the MD simulations were performed under the *NPT* ensemble for 10 ns. For the validation of the molecular dynamic simulation, a 100 ns MD simulation were performed and graphs values were collected to extract the graphs of root-mean-square deviations (RMSD) and root-mean-square fluctuations (RMSFs). The graphs were plotted using raw data obtained from DESMONDs and MS excel. The trajectories of MD simulation were analyzed through simulation event analysis, simulation quality analysis, which were then further studied in the Simulation Interaction Diagram tool in Maestro.

5.11. Chicken CAM Assay. *5.11.1. CAM Assay Protocol.* In order to further validate the results obtained from bioinformatic analysis, a chicken CAM assay was utilized for the preclinical evaluation of the identified target. The fertilized chicken eggs were incubated at 37 °C with 50−60% humidity. The embryo handling, study design, and experimental procedures were identical to those described in section 2.1. On the ninth day, the CAMs were harvested, formalin-fixed, and subsequently used for stereoscopic evaluation and EGFR expression using IHC staining.

5.11.2. Evaluation of Angiogenesis. The fixed membranes were observed in the stereoscope. Stereoscopic images were captured by LMI stereoscope mounted with a 12MP Sony Exmor CMOS sensor camera. The images were processed in ImageJ software for calculation of the total vessel area. The percentage inhibition in the vessel area was calculated by the following formula:

$$\text{Percentage inhibition} = \frac{N(\text{Control}) - N(\text{Treated})}{N(\text{Control})} \times 100$$

where N(Control) = vessel area obtained from ImageJ in the control group and N(Treatment) = vessel area obtained from ImageJ in the treated group

5.12. Immunohistochemical Staining. The immunohistochemical (IHC) staining was performed to determine the expression of EGFR in the CAM membranes. EGFR staining was carried out using EGFR Leica biosystems in accordance with the manufacturer's instructions and with the reagents included in the kits. Briefly, the tissue slices were embedded in melted wax at a high temperature prior to sectioning at a thickness of 5 μm. Tissues were deparaffinized in xylene and rehydrated in a series of graded alcohol concentrations. After deparaffinization and rehydration, antigen retrieval was

https://doi.org/10.1021/acsomega.2c07570
ACS Omega 2023, 8, 14985−15002

conducted for 5 min using a proteinase K solution. The activity of endogenous peroxidase was inhibited for 15 min by 3% hydrogen peroxide. The sections were then washed with the buffer provided. Slides were placed in a humid chamber and incubated with primary anti-EGFR mAb for 30 min. Tissue sections were rinsed three times with PBS (10 min per rinse) and then incubated with a detection system for 30 min. All tissue sections were treated with 3,3′-diaminobenzidine for 5 min and rinsed three times with deionized water to observe antibody staining. The sections were counterstained for 5 min with hematoxylin. The portions were then washed gently with water for 5 min, dehydrated, and sealed with a cover slide. Figure 11 depicts a summary of the target fishing and validation approach.

5.13. Statistical Analysis. The semiquantitative scores and vessel area were analyzed by ordinary one way Analysis of Variance ANNOVA. The results of the treated groups were compared with the controls using Dunnett's multiple comparisons test, with a single pooled variance.

■ ASSOCIATED CONTENT

Supporting Information

The Supporting Information is available free of charge at https://pubs.acs.org/doi/10.1021/acsomega.2c07570.

Network constructed by using string database; protein secondary structure elements (SSE) after MD simulation; torison angles of saroglitazar with EGFR; ligand RMSD, radius of gyration (rGyr), intramolecular hydrogen bonds, molecular surface area (MolSA), solvent accessible surface area (SASA), polar surface area (PSA) of EGFR-Saroglitazar complex; centrality parameters of hub targets in Protein Interaction Network; abbreviation and full names of the hub genes (PDF)

■ AUTHOR INFORMATION

Corresponding Author

Nilanjan Saha − *Centre for Translational and Clinical Research, School of Chemical and Life Science, Jamia Hamdard University, New Delhi 110062, India;* orcid.org/0000-0003-1564-0142; Phone: 9873013366; Email: nilanjan.saha@jamiahamdard.ac.in

Authors

Swarna Dabral − *Department of Pharmacology, School of Pharmaceutical Education and Research, Jamia Hamdard, New Delhi 110062, India*

Imran Ahmd Khan − *Department of Chemistry, School of Chemical and Life Science, Jamia Hamdard, New Delhi 110062, India;* orcid.org/0000-0002-2014-4277

Tarun Pant − *Department of Medicine, Medical College of Wisconsin, Milwaukee, Wisconsin 53226, United States*

Sabina Khan − *Department of Pathology, Hamdard Institute of Medical Sciences and Research, Jamia Hamdard, New Delhi 110062, India*

Prem Prakash − *Protein Assembly Laboratory, JH-Institute of Molecular Medicine, Jamia Hamdard University, New Delhi 110062, India*

Suhel Parvez − *Department of Medical Elementology and Toxicology, School of Chemical and Life Science, Jamia Hamdard University, New Delhi 110062, India;* orcid.org/0000-0002-6318-6506

Complete contact information is available at: https://pubs.acs.org/10.1021/acsomega.2c07570

Author Contributions

S.D. performed the experiments, interpreted data and drafted the manuscript. The figures in the manuscript, including TOC were created by S.D. I.A.K. conceptualized the study, provided resources for the project administration and reviewed the manuscript, T.P. conceptualized the experiments, drafted the original article and reviewed the draft. S.K. provided guidance and support in performing and analyzing histopathological analysis. P.P. provided support and facility for execution of the bioinformatics work. S.P. provide the facility and support on experimental design and manuscript preparation. N.S. provided advice on experimental design and supervised the project and gave final approval of the manuscript.

Notes

The authors declare no competing financial interest.

■ ACKNOWLEDGMENTS

This project has received funding from the Division of Innovation and Translational Research, Indian Council of Medical Research (ICMR) Government of India, by providing Senior Research Fellowship to S.D. in accordance with project file number 5/3/8/29/ITR-F/2019-ITR. P.P. is supported by Science and Engineering Research Board, Department of Science and Technology (ECR/2017/000235 and EEQ/2020/000299), Indian Council of Medical Research (ICMR) ((P-12)ITR/Adhoc/18/2020), Government of India and Ministry of Science & Technology Department of Biotechnology, Government of India, No. BT/RLF/Re-Entry/24/2015. S.P. is Supported by Department of Science and Technology (DST), Promotion of University Research and Scientific Excellence (PURSE), Government of India.

■ REFERENCES

(1) Pant, T.; Dhanasekaran, A.; Bai, X.; Zhao, M.; Thorp, E. B.; Forbess, J. M.; Bosnjak, Z. J.; Ge, Z.-D. Genome-Wide Differential Expression Profiling of LncRNAs and MRNAs Associated with Early Diabetic Cardiomyopathy. *Sci. Rep* **2019**, *9* (1), 15345.

(2) Pant, T.; Dhanasekaran, A.; Fang, J.; Bai, X.; Bosnjak, Z. J.; Liang, M.; Ge, Z.-D. Current Status and Strategies of Long Noncoding RNA Research for Diabetic Cardiomyopathy. *BMC Cardiovasc Disord* **2018**, *18* (1), 197.

(3) Pant, T.; Dhanasekaran, A.; Zhao, M.; Thorp, E. B.; Forbess, J. M.; Bosnjak, Z. J.; Benjamin, I. J.; Ge, Z.-D. Identification and Analysis of Circulating Long Non-Coding RNAs with High Significance in Diabetic Cardiomyopathy. *Sci. Rep* **2021**, *11* (1), 2571.

(4) Pant, T.; Mishra, M. K.; Bai, X.; Ge, Z.-D.; Bosnjak, Z. J.; Dhanasekaran, A. Microarray Analysis of Long Non-Coding RNA and MRNA Expression Profiles in Diabetic Cardiomyopathy Using Human Induced Pluripotent Stem Cell−Derived Cardiomyocytes. *Diab Vasc Dis Res.* **2019**, *16* (1), 57−68.

(5) Advani, A.; Wiggins, K. J.; Cox, A. J.; Zhang, Y.; Gilbert, R. E.; Kelly, D. J. Inhibition of the Epidermal Growth Factor Receptor Preserves Podocytes and Attenuates Albuminuria in Experimental Diabetic Nephropathy: EGFR Inhibition in Diabetic Nephropathy. *Nephrology* **2011**, *16* (6), 573−581.

(6) Blaine, S. A.; Ray, K. C.; Branch, K. M.; Robinson, P. S.; Whitehead, R. H.; Means, A. L. Epidermal Growth Factor Receptor Regulates Pancreatic Fibrosis. *Am. J. Physiol Gastrointest Liver Physiol* **2009**, *297* (3), G434−G441.

(7) Fadini, G. P.; Albiero, M.; Bonora, B. M.; Avogaro, A. Angiogenic Abnormalities in Diabetes Mellitus: Mechanistic and

Clinical Aspects. *J. Clin Endocrinol Metab* **2019**, *104* (11), 5431−5444.
(8) Joharapurkar, A.; Patel, V.; Kshirsagar, S.; Patel, M. S.; Savsani, H.; Jain, M. Effect of Dual PPAR-α/γ Agonist Saroglitazar on Diabetic Retinopathy and Oxygen-Induced Retinopathy. *Eur. J. Pharmacol.* **2021**, *899*, 174032.
(9) Tahergorabi, Z.; Khazaei, M. Imbalance of Angiogenesis in Diabetic Complications: The Mechanisms. *Int. J. Prev Med.* **2012**, *3* (12), 827.
(10) Cui, Q.; Ma, Y.; Jaramillo, M.; Bari, H.; Awan, A.; Yang, S.; Zhang, S.; Liu, L.; Lu, M.; O'Connor-McCourt, M.; Purisima, E. O.; Wang, E. A Map of Human Cancer Signaling. *Mol. Syst. Biol.* **2007**, *3* (1), 152.
(11) DeGorter, M. K.; Xia, C. Q.; Yang, J. J.; Kim, R. B. Drug Transporters in Drug Efficacy and Toxicity. *Annu. Rev. Pharmacol. Toxicol.* **2012**, *52* (1), 249−273.
(12) Giovannucci, E.; Harlan, D. M.; Archer, M. C.; Bergenstal, R. M.; Gapstur, S. M.; Habel, L. A.; Pollak, M.; Regensteiner, J. G.; Yee, D. Diabetes and Cancer: A Consensus Report. *CA Cancer J. Clin* **2010**, *60* (4), 207−221.
(13) Hanahan, D.; Weinberg, R. A. Hallmarks of Cancer: The Next Generation. *Cell* **2011**, *144* (5), 646−674.
(14) Hornberg, J. J.; Bruggeman, F. J.; Westerhoff, H. V.; Lankelma, J. Cancer: A Systems Biology Disease. *Biosystems* **2006**, *83* (2−3), 81−90.
(15) Xie, T.; Song, S.; Li, S.; Ouyang, L.; Xia, L.; Huang, J. Review of Natural Product Databases. *Cell Prolif.* **2015**, *48* (4), 398−404.
(16) Wei, H.; Liu, S.; Liao, Y.; Ma, C.; Wang, D.; Tong, J.; Feng, J.; Yi, T.; Zhu, L. A Systematic Review of the Medicinal Potential of Mulberry in Treating Diabetes Mellitus. *Am. J. Chin Med.* **2018**, *46* (08), 1743−1770.
(17) Chen, Q.; Zhu, L.; Tang, Y.; Zhao, Z.; Yi, T.; Chen, H. Preparation-Related Structural Diversity and Medical Potential in the Treatment of Diabetes Mellitus with Ginseng Pectins: Ginseng Pectins Treating Diabetes Mellitus. *Ann. N.Y. Acad. Sci.* **2017**, *1401* (1), 75−89.
(18) Ng, K.-W.; Cao, Z.-J.; Chen, H.-B.; Zhao, Z.-Z.; Zhu, L.; Yi, T. Oolong Tea: A Critical Review of Processing Methods, Chemical Composition, Health Effects, and Risk. *Crit Rev. Food Sci. Nutr* **2018**, *58* (17), 2957−2980.
(19) Zhu, B.; Qu, S. The Relationship Between Diabetes Mellitus and Cancers and Its Underlying Mechanisms. *Front Endocrinol* **2022**, *13*, 800995.
(20) Felmeden, D. Angiogenesis: Basic Pathophysiology and Implications for Disease. *Eur. Heart J.* **2003**, *24* (7), 586−603.
(21) Ribatti, D.; Annese, T.; Ruggieri, S.; Tamma, R.; Crivellato, E. Limitations of Anti-Angiogenic Treatment of Tumors. *Transl Oncol* **2019**, *12* (7), 981−986.
(22) Andorf, C. M.; Honavar, V.; Sen, T. Z. Predicting the Binding Patterns of Hub Proteins: A Study Using Yeast Protein Interaction Networks. *PLoS One* **2013**, *8* (2), No. e56833.
(23) Kennedy, D. C.; Coen, B.; Wheatley, A. M.; McCullagh, K. J. A. Microvascular Experimentation in the Chick Chorioallantoic Membrane as a Model for Screening Angiogenic Agents Including from Gene-Modified Cells. *IJMS* **2022**, *23* (1), 452.
(24) Lin, T.-C. Gefitinib Modulates Stress Fibers and Tubular-like Structure Formation and Attenuates Angiogenesis in an in Vivo Chicken Model of Chorioallantoic Membrane Angiogenesis. *Biochem. Biophys. Res. Commun.* **2020**, *526* (3), 568−573.
(25) Avram, S.; Ghiulai, R.; Pavel, I. Z.; Mioc, M.; Babuta, R.; Voicu, M.; Coricovac, D.; Danciu, C.; Dehelean, C.; Soica, C. Phytocompounds Targeting Cancer Angiogenesis Using the Chorioallantoic Membrane Assay. In *Natural Products and Cancer Drug Discovery*; IntechOpen, 2017. https://www.intechopen.com/chapters/55790.
(26) Macalino, S. J. Y.; Gosu, V.; Hong, S.; Choi, S. Role of Computer-Aided Drug Design in Modern Drug Discovery. *Arch. Pharm. Res.* **2015**, *38* (9), 1686−1701.
(27) Ba, Q.; Li, J.; Huang, C.; Li, J.; Chu, R.; Wu, Y.; Wang, H. Topological, Functional, and Dynamic Properties of the Protein Interaction Networks Rewired by Benzo(a)Pyrene. *Toxicol. Appl. Pharmacol.* **2015**, *283* (2), 83−91.
(28) Barabási, A.-L.; Oltvai, Z. N. Network Biology: Understanding the Cell's Functional Organization. *Nat. Rev. Genet* **2004**, *5* (2), 101−113.
(29) Karar, J.; Maity, A. PI3K/AKT/MTOR Pathway in Angiogenesis. *Front. Mol. Neurosci.* **2011**, *4*, 4.
(30) Xiao, X.; Wang, W.; Li, Y.; Yang, D.; Li, X.; Shen, C.; Liu, Y.; Ke, X.; Guo, S.; Guo, Z. HSP90AA1-Mediated Autophagy Promotes Drug Resistance in Osteosarcoma. *J. Exp Clin Cancer Res.* **2018**, *37* (1), 201.
(31) Ahsan, A.; Ramanand, S. G.; Whitehead, C.; Hiniker, S. M.; Rehemtulla, A.; Pratt, W. B.; Jolly, S.; Gouveia, C.; Truong, K.; Waes, C. V.; Ray, D.; Lawrence, T. S.; Nyati, M. K. Wild-Type EGFR Is Stabilized by Direct Interaction with HSP90 in Cancer Cells and Tumors. *Neoplasia* **2012**, *14* (8), 670−IN1.
(32) Rong, B.; Yang, S. Molecular Mechanism and Targeted Therapy of Hsp90 Involved in Lung Cancer: New Discoveries and Developments (Review). *Int. J. Oncol.* **2017**, DOI: 10.3892/ijo.2017.4214.
(33) Tsang, R. Y.; Sadeghi, S.; Finn, R. S. Lapatinib, a Dual-Targeted Small Molecule Inhibitor of EGFR and HER2, in HER2-Amplified Breast Cancer: From Bench to Bedside. *Clin. Med. Insights: Ther.* **2011**, *3*, CMT.S3783.
(34) Yang, S.-C.; Chang, S.-S.; Chen, H.-Y.; Chen, C. Y.-C. Identification of Potent EGFR Inhibitors from TCM Database@Taiwan. *PLoS Comput. Biol.* **2011**, *7* (10), No. e1002189.
(35) Abourehab, M. A. S.; Alqahtani, A. M.; Youssif, B. G. M.; Gouda, A. M. Globally Approved EGFR Inhibitors: Insights into Their Syntheses, Target Kinases, Biological Activities, Receptor Interactions, and Metabolism. *Molecules* **2021**, *26* (21), 6677.
(36) Kannangai, R.; Sahin, F.; Torbenson, M. S. EGFR Is Phosphorylated at Ty845 in Hepatocellular Carcinoma. *Mod. Pathol* **2006**, *19* (11), 1456−1461.
(37) Tong, J.; Taylor, P.; Peterman, S. M.; Prakash, A.; Moran, M. F. Epidermal Growth Factor Receptor Phosphorylation Sites Ser991 and Tyr998 Are Implicated in the Regulation of Receptor Endocytosis and Phosphorylations at Ser1039 and Thr1041. *Mol. Cell Proteomics* **2009**, *8* (9), 2131−2144.
(38) Li, D.-D.; Wu, T.-T.; Yu, P.; Wang, Z.-Z.; Xiao, W.; Jiang, Y.; Zhao, L.-G. Molecular Dynamics Analysis of Binding Sites of Epidermal Growth Factor Receptor Kinase Inhibitors. *ACS Omega* **2020**, *5* (26), 16307−16314.
(39) Lin, T.-C. Gefitinib Modulates Stress Fibers and Tubular-like Structure Formation and Attenuates Angiogenesis in an in Vivo Chicken Model of Chorioallantoic Membrane Angiogenesis. *Biochem. Biophys. Res. Commun.* **2020**, *526* (3), 568−573.
(40) Advani, A.; Wiggins, K. J.; Cox, A. J.; Zhang, Y.; Gilbert, R. E.; Kelly, D. J. Inhibition of the Epidermal Growth Factor Receptor Preserves Podocytes and Attenuates Albuminuria in Experimental Diabetic Nephropathy: EGFR Inhibition in Diabetic Nephropathy. *Nephrology* **2011**, *16* (6), 573−581.
(41) Brandt, S.; Mertens, P. R. Epidermal Growth Factor Receptor Mediates Injury in Rapidly Progressive Glomerular Disease. *Int. Urol Nephrol* **2012**, *44* (3), 971−975.
(42) Panchapakesan, U.; Pollock, C.; Saad, S. Renal Epidermal Growth Factor Receptor: Its Role in Sodium and Water Homeostasis in Diabetic Nephropathy: EGFR in Kidney Sodium and Water Regulation. *Clin. Exp. Pharmacol. Physiol.* **2011**, *38* (2), 84−88.
(43) Akhtar, S.; Yousif, M. H. M.; Chandrasekhar, B.; Benter, I. F. Activation of EGFR/ERBB2 via Pathways Involving ERK1/2, P38 MAPK, AKT and FOXO Enhances Recovery of Diabetic Hearts from Ischemia-Reperfusion Injury. *PLoS One* **2012**, *7* (6), No. e39066.
(44) Belmadani, S.; Palen, D. I.; Gonzalez-Villalobos, R. A.; Boulares, H. A.; Matrougui, K. Elevated Epidermal Growth Factor Receptor Phosphorylation Induces Resistance Artery Dysfunction in Diabetic Db/Db Mice. *Diabetes* **2008**, *57* (6), 1629−1637.
(45) Li, Y.; Pan, Y.; Cao, S.; Sasaki, K.; Wang, Y.; Niu, A.; Fan, X.; Wang, S.; Zhang, M.-Z.; Harris, R. C. Podocyte EGFR Inhibits

https://doi.org/10.1021/acsomega.2c07570
ACS Omega 2023, 8, 14985−15002

Autophagy Through Upregulation of Rubicon in Type 2 Diabetic Nephropathy. *Diabetes* **2021**, *70* (2), 562−576.
(46) Rodriguez, C. Diabetes and Risk of Prostate Cancer in a Prospective Cohort of US Men. *Am. J. Epidemiol* **2005**, *161* (2), 147−152.
(47) Davila, J. A. Diabetes Increases the Risk of Hepatocellular Carcinoma in the United States: A Population Based Case Control Study. *Gut* **2005**, *54* (4), 533−539.
(48) Huxley, R.; Ansary-Moghaddam, A.; Berrington de González, A.; Barzi, F.; Woodward, M. Type-II Diabetes and Pancreatic Cancer: A Meta-Analysis of 36 Studies. *Br. J. Cancer* **2005**, *92* (11), 2076−2083.
(49) Inoue, M. Diabetes Mellitus and the Risk of Cancer: Results From a Large-Scale Population-Based Cohort Study in Japan. *Arch Intern Med.* **2006**, *166* (17), 1871.
(50) Rousseau, M.-C.; Parent, M.-É.; Pollak, M. N.; Siemiatycki, J. Diabetes Mellitus and Cancer Risk in a Population-Based Case-Controlstudy among Men from Montreal, Canada: Diabetes Mellitus and Cancer Risk in a Population-Based Case-Control Study. *Int. J. Cancer* **2006**, *118* (8), 2105−2109.
(51) Seow, A.; Yuan, J.-M.; Koh, W.-P.; Lee, H.-P.; Yu, M. C. Diabetes Mellitus and Risk of Colorectal Cancer in the Singapore Chinese Health Study. *JNCI: J. Natl. Cancer Inst* **2006**, *98* (2), 135−138.
(52) Moiseeva, O.; Xavier-Deschênes-Simard; Pollak, M.; Ferbeyre, G. Metformin, Aging and Cancer. *Aging* **2013**, *5* (5), 330−331.
(53) Cui, Q.; Ma, Y.; Jaramillo, M.; Bari, H.; Awan, A.; Yang, S.; Zhang, S.; Liu, L.; Lu, M.; O'Connor-McCourt, M.; Purisima, E. O.; Wang, E. A Map of Human Cancer Signaling. *Mol. Syst. Biol.* **2007**, *3* (1), 152.
(54) Stewart, A. K. How Thalidomide Works Against Cancer. *Science* **2014**, *343* (6168), 256−257.
(55) Beedie, S. L.; Mahony, C.; Walker, H. M.; Chau, C. H.; Figg, W. D.; Vargesson, N. Shared Mechanism of Teratogenicity of Anti-Angiogenic Drugs Identified in the Chicken Embryo Model. *Sci. Rep* **2016**, *6* (1), 30038.
(56) Ribatti, D. The Chick Embryo Chorioallantoic Membrane (CAM) Assay. *Reprod. Toxicol.* **2017**, *70*, 97−101.
(57) Miller, W. J.; Kayton, M. L.; Patton, A.; O'Connor, S.; He, M.; Vu, H.; Baibakov, G.; Lorang, D.; Knezevic, V.; Kohn, E.; Alexander, H. R.; Stirling, D.; Payvandi, F.; Muller, G. W.; Libutti, S. K. A Novel Technique for Quantifying Changes in Vascular Density, Endothelial Cell Proliferation and Protein Expression in Response to Modulators of Angiogenesis Using the Chick Chorioallantoic Membrane (CAM) Assay. *J. Transl Med.* **2004**, *2* (1), 4.
(58) Daina, A.; Michielin, O.; Zoete, V. SwissTargetPrediction: Updated Data and New Features for Efficient Prediction of Protein Targets of Small Molecules. *Nucleic Acids Res.* **2019**, *47* (W1), W357−W364.
(59) Gfeller, D.; Michielin, O.; Zoete, V. Shaping the Interaction Landscape of Bioactive Molecules. *Bioinformatics* **2013**, *29* (23), 3073−3079.
(60) Chen, X. TTD: Therapeutic Target Database. *Nucleic Acids Res.* **2002**, *30* (1), 412−415.
(61) Wishart, D. S.; Feunang, Y. D.; Guo, A. C.; Lo, E. J.; Marcu, A.; Grant, J. R.; Sajed, T.; Johnson, D.; Li, C.; Sayeeda, Z.; Assempour, N.; Iynkkaran, I.; Liu, Y.; Maciejewski, A.; Gale, N.; Wilson, A.; Chin, L.; Cummings, R.; Le, D.; Pon, A.; Knox, C.; Wilson, M. DrugBank 5.0: A Major Update to the DrugBank Database for 2018. *Nucleic Acids Res.* **2018**, *46* (D1), D1074−D1082.
(62) Piñero, J.; Ramírez-Anguita, J. M.; Saüch-Pitarch, J.; Ronzano, F.; Centeno, E.; Sanz, F.; Furlong, L. I. The DisGeNET Knowledge Platform for Disease Genomics: 2019 Update. *Nucleic Acids Res.* **2019**, gkz1021.
(63) The UniProt Consortium. UniProt: A Hub for Protein Information. *Nucleic Acids Res.* **2015**, *43* (D1), D204−D212.
(64) *Bioinformatics & Evolutionary Genomics: Draw Venn Diagram (ugent.be)* available at https://bioinformatics.psb.ugent.be/webtools/Venn/.
(65) Szklarczyk, D.; Gable, A. L.; Nastou, K. C.; Lyon, D.; Kirsch, R.; Pyysalo, S.; Doncheva, N. T.; Legeay, M.; Fang, T.; Bork, P.; Jensen, L. J.; von Mering, C. The STRING Database in 2021: Customizable Protein-Protein Networks, and Functional Characterization of User-Uploaded Gene/Measurement Sets. *Nucleic Acids Res.* **2021**, *49* (D1), D605−D612.
(66) Ge, S. X.; Jung, D.; Yao, R. ShinyGO: A Graphical Gene-Set Enrichment Tool for Animals and Plants. *Bioinformatics* **2020**, *36* (8), 2628−2629.
(67) Goodsell, D. S.; Dutta, S.; Zardecki, C.; Voigt, M.; Berman, H. M.; Burley, S. K. The RCSB PDB "Molecule of the Month": Inspiring a Molecular View of Biology. *PLoS Biol.* **2015**, *13* (5), No. e1002140.
(68) Minder, P.; Zajac, E.; Quigley, J. P.; Deryugina, E. I. EGFR Regulates the Development and Microarchitecture of Intratumoral Angiogenic Vasculature Capable of Sustaining Cancer Cell Intravasation. *Neoplasia* **2015**, *17* (8), 634−649.

https://doi.org/10.1021/acsomega.2c07570
ACS Omega 2023, 8, 14985−15002